crystals

MDPI

*Article*

# The Comparative Study of Four Hexachloroplatinate, Tetrachloroaurate, Tetrachlorocuprate, and Tetrabromocuprate Benzyltrimethylammonium Salts: Synthesis, Single-Crystal X-Ray Structures, Non-Classical Synthon Preference, Hirshfeld Surface Analysis, and Quantum Chemical Study

**Joanna Bojarska [1,*], Martin Breza [2], Ingrid Jelemenska [2], Izabela D. Madura [3], Sepideh Jafari [1], Damian Trzybiński [4], Krzysztof Woźniak [4] and Adam Mieczkowski [5,*]**

1 Chemistry Department, Institute of Ecological and Inorganic Chemistry, Technical University of Lodz, 116 Zeromskiego, 90-924 Lodz, Poland; sepideh.jafari@dokt.p.lodz.pl
2 Department of Physical Chemistry, Slovak Technical University, Radlinskeho 9, 81237 Bratislava, Slovakia; martin.breza@stuba.sk (M.B.); ingrid.jelemenska@stuba.sk (I.J.)
3 Faculty of Chemistry, Warsaw University of Technology, 3 Noakowskiego, 00-664 Warsaw, Poland; izabela.madura@pw.edu.pl
4 Biological and Chemical Research Centre, University of Warsaw, Żwirki i Wigury 101, 02-089 Warsaw, Poland; dtrzybinski@cnbc.uw.edu.pl (D.T.); kwozniak@chem.uw.edu.pl (K.W.)
5 Institute of Biochemistry and Biophysics, Polish Academy of Sciences, Pawinskiego 5a, 02-106 Warsaw, Poland
* Correspondence: joanna.bojarska@p.lodz.pl (J.B.); amiecz@ibb.waw.pl (A.M.)

## Abstract

Four benzyltrimethylammonium (BTMA) salts were successfully prepared: bis(benzyltrimethylammonium) hexachloroplatinate (**1**), benzyltrimethylammonium tetrachloroaurate (**2**), bis(benzyltrimethylammonium) tetrachlorocuprate (**3**), and bis(benzyltrimethylammonium) tetrabromocuprate (**4**) from benzyltrimethylammonium hydroxide (Triton B). Their crystal structures were determined by single-crystal X-ray diffraction, and the supramolecular architectures were characterized hierarchically. Extended Hirshfeld surface analysis, including enrichment ratio calculations, was performed to evaluate intermolecular interactions. Nonclassical hydrogen bonds, such as C–H···Cl(Br), involving the anions, contribute to the formation of self-assembled architectures. Additional stabilization arises from π···π and Cu–Br···π interactions, particularly in crystals **2** and **4**, respectively. Hirshfeld surface analysis showed that H···H and C···H/H···C interactions are the dominant contributors in all crystals. According to enrichment ratio calculations, C···H/H···C interactions in **1**, **3**, and **4**; Cl···H/H···Cl in **1** and **3**; Cu···H/H···Cu in **3** and **4**; and Br···H/H···Br and Br···C/C···Br in **4** are statistically favored in the crystal packing. Halogen bonding Cl···Cl was observed in **1** but does not significantly influence packing. Energy framework calculations indicated that dispersive interactions are favorable in the analyzed crystals. A library of H-bonding supramolecular patterns, including interchangeable synthons, is provided and may guide the rational design of new derivatives with controllable features. Finally, the topology of intermolecular connections and the electronic structure of the benzyltrimethylammonium cation, investigated by quantum-chemical calculations, provide insights into its reactivity.

**Keywords:** benzyltrimethylammonium salts; synthesis; crystal structure; non-classical H-bonding; halogen bonding; supramolecular architecture; synthon; Hirshfeld surface; enrichment ratio; energy framework; MP2 calculations



Academic Editor: Aidar T. Gubaidullin

Received: 29 October 2025
Revised: 3 December 2025
Accepted: 8 December 2025
Published: 11 December 2025

**Citation:** Bojarska, J.; Breza, M.; Jelemenska, I.; Madura, I.D.; Jafari, S.; Trzybiński, D.; Woźniak, K.; Mieczkowski, A. The Comparative Study of Four Hexachloroplatinate, Tetrachloroaurate, Tetrachlorocuprate, and Tetrabromocuprate Benzyltrimethylammonium Salts: Synthesis, Single-Crystal X-Ray Structures, Non-Classical Synthon Preference, Hirshfeld Surface Analysis, and Quantum Chemical Study. *Crystals* **2025**, *15*, 1051. https://doi.org/10.3390/cryst15121051

## 1. Introduction

Hybrid organic–inorganic halometallates, possessing organic, quaternary ammonium cations and inorganic metal-containing anions, could find significant importance in material sciences, chemistry, and crystal engineering. These compounds, such as 1-ethyl-3-methylimidazolium tetrachloroaurate, could be used as low-temperature ionic liquids, exhibiting ionic liquid behavior from 58 to 220 °C with possible applications in catalysis and electrochemical technologies [1]. The formation of tetrachloroaurate salts from gold(III) chloride and tetraalkylammonium chlorides facilitates the extraction of gold from water solutions to the organic phase [2]. Appropriate salts obtained from hexadecyltrimethylammonium hydroxide and hexachloroplatinic or tetrachloroauric acid were used for the synthesis of nanoparticles and nanofibers on HOPG (highly oriented pyrolytic graphite) [3]. Three hexachloroplatinate complexes $[(C_2H_5)_2NH_2]_2[PtCl_6]$, $[(C_2H_5)_4N]_2[PtCl_6]$, and $[(CH_3)_3NH]_2[PtCl_6]$ were synthetized and tested for their antibacterial activities against *Escherichia coli* strain M-17. A reliable antimicrobial effect was observed for the latter compound [4]. Organic tetrachlorocuprate salts exhibited termochromic properties [5,6] and possess promising antibacterial activities [7,8]. Another example of such compounds is trimethylchloromethylammonium tetrachloroferrate, a plastic crystal capable of magnetic-optic-electric triple switching and thermal energy storage [9]. Finally, a magnetic ionic liquid—1-butyl-3-methylimidazolium tetrachloroferrate—was obtained and its magnetic behavior and susceptibility was investigated [10].

Crystal engineering focuses on the employment of intermolecular interactions, including hydrogen/halogen bonding, π-based interactions, and electrostatic, hydrophobic, and van der Waals interactions, to self-assemble crystalline materials with controllable properties [11,12]. Hydrogen bonds are, without a doubt, the most popular interactions driving self-assembled structures (supramolecules). Halogen bonding and other non-classical interactions, which play a significant role in supramolecular structures, have occasionally been reported in the scientific literature.

In a continuation of our supramolecular explorations of organic salts [13–15], in the present manuscript, we report the synthesis and thorough supramolecular investigation of four salts, namely, bis(benzyltrimethylammonium) hexachloroplatinate (**1**), benzyltrimethylammonium tetrachloroaurate (**2**), bis(benzyltrimethylammonium) tetrachlorocuprate (**3**), and bis(benzyltrimethylammonium) tetrabromocuprate (**4**), as shown in Scheme 1. It is interesting to note that the supramolecular architectures of these structures are formed only by non-classical interactions. The nature and topology of these interactions are studied by an extended Hirshfeld surface analysis and energy frameworks. The supramolecular preferences of synthetized salts were investigated, and a library of H-bonding supramolecular synthons was developed. Furthermore, quantum chemical studies of compounds containing benzyltrimethylammonium cations, $BTMA^+$, are of two types. Luminescence [16] and magnetic properties [17] were investigated using periodic DFT calculations of the entire crystal (including anions). On the other hand, the vibrational spectra of a crystal were assigned by DFT calculations of the sole $BTMA^+$ [18]. The same holds for DFT studies of $BTMA^+$ degradation by hydroxides' [19–21] adsorption on electrodes [22,23] and catalysis [24]. None of the above studies deals with a detailed study of the electronic structure of $BTMA^+$, which should explain some of its physical and chemical properties. Thus, we will address this omission.

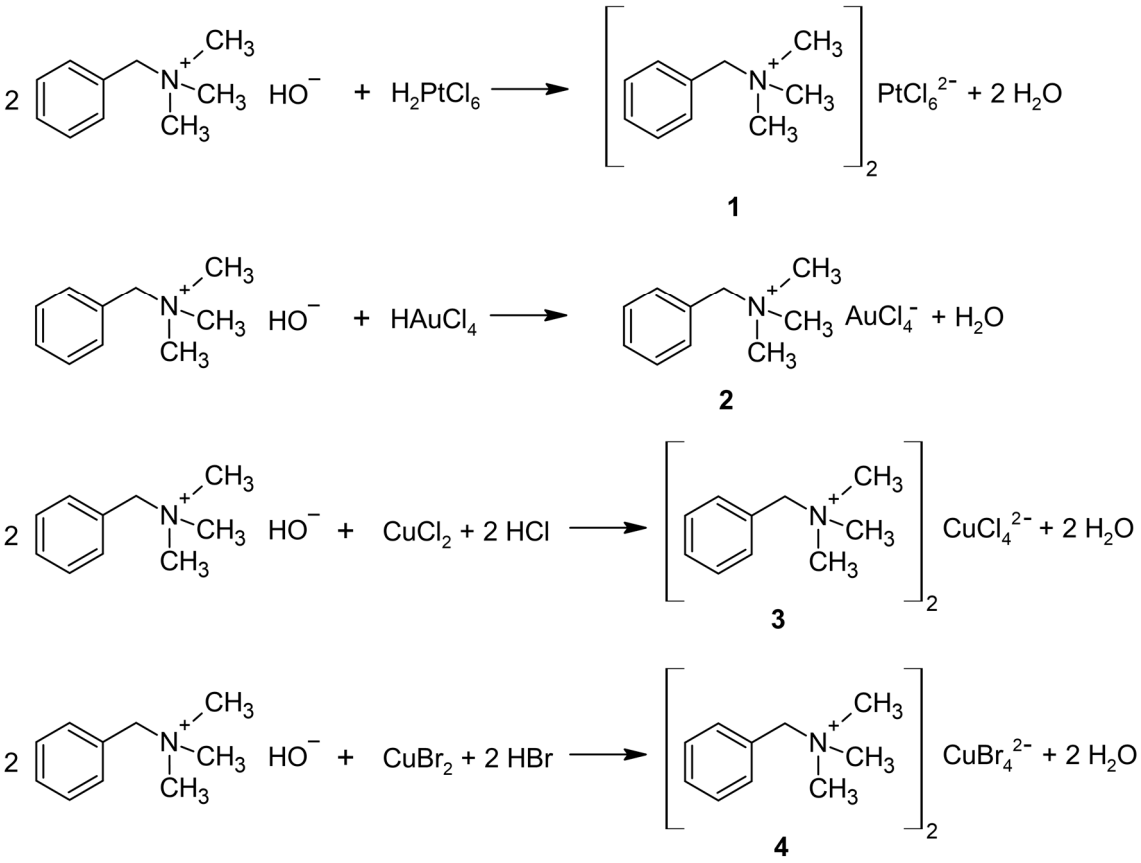


**Scheme 1.** The synthesis of the analyzed salts: bis(benzyltrimethylammonium) hexachloroplatinate (**1**), benzyltrimethylammonium tetrachloroaurate (**2**), bis(benzyltrimethylammonium) tetrachlorocuprate (**3**), and bis(benzyltrimethylammonium) tetrabromocuprate (**4**).

The crystal structures of bis(benzyltrimethylammonium) tetrachlorocuprate (**3**) and bis(benzyltrimethylammonium) tetrabromocuprate (**4**) have been reported previously [25,26]; however, they were determined at room temperature, and those studies do not provide a comprehensive analysis of their supramolecular features, including the intermolecular interactions that govern the crystal packing. Moreover, no quantum–mechanical calculations were carried out (in the case of **3** this is understandable, because its crystal structure was described in the 1960s). In view of these limitations, the aim of the present work was to deliver a more complete structural and theoretical description of these systems, with particular emphasis on their supramolecular organization and the nature of the interactions stabilizing the crystal structures. Additionally, a polymorphic form ($P2_1/c$) of **3** was also described in the literature [27].

## 2. Materials and Methods

### *2.1. Preparation of Salts **1**–**4***

Bis(benzyltrimethylammonium) hexachloroplatinate (**1**): To 1.37 g of a 30% solution of hexachloroplatinic acid $H_2PtCl_6$ in water (410 mg of $H_2PtCl_6$, 1 mmol, 1 equiv.), diluted with 2 mL of distilled water, 824 mg of a 40% solution of benzyltrimethylammonium hydroxide (Triton B, 2 mmol, 2 equiv.) in methanol, diluted with 2 mL of distilled water, was added dropwise and vigorously stirred at room temperature for 5 min. The slow evaporation of the obtained solution in room temperature led to the formation of **1** crystals.

Benzyltrimethylammonium tetrachloroaurate (**2**): To 1.13 g of a 30% solution of tetrachloroauric acid $HAuCl_4$ in water (340 mg of $HAuCl_4$, 1 mmol, 1 equiv.), diluted with 2 mL of distilled water, 418 mg of a 40% solution of benzyltrimethylammonium hydroxide (1 mmol, 1 equiv.) in methanol, diluted with 2 mL of distilled water, was added dropwise and

vigorously stirred in room temperature for 5 min. The slow evaporation of the obtained solution at room temperature led to the formation of **2** crystals.

Bis(benzyltrimethylammonium) tetrachlorocuprate (**3**): To 135 mg of copper(II) chloride $CuCl_2$ in 2 mL of distilled water, 200 µL of a 37% solution of hydrochloric acid in water (73 mg of HCl, 2 mmol, 2 equiv.) was added, followed by 824 mg of a 40% solution of benzyltrimethylammonium hydroxide (2 mmol, 2 equiv.) diluted with 2 mL of distilled water, and the obtained solution was vigorously stirred at room temperature for 5 min. The slow evaporation at room temperature led to the formation of **3** crystals.

Bis(benzyltrimethylammonium) tetrabromocuprate (**4**): To 223 mg of copper(II) bromide $CuBr_2$ in 2 mL of distilled water, 404 µL of a 40% solution of hydrobromic acid in water (162 mg of HBr, 2 mmol, 2 equiv.) was added, followed by 824 mg of a 40% solution of benzyltrimethylammonium hydroxide (2 mmol, 2 equiv.) diluted with 2 mL of distilled water, and the obtained solution was vigorously stirred at room temperature for 5 min. The slow evaporation at room temperature led to the formation of **4** crystals.

### *2.2. Crystallography*

Good quality single crystals of the investigated compounds were selected for the X-ray diffraction experiments at $T$ = 100(2) K. Diffraction data were collected on the Agilent Technologies (Santa Clara, CA, USA) SuperNova Double Source diffractometer with Cu$K\alpha$ ($\lambda$ = 1.54184 Å) radiation (**1**, **3,** and **4**) and the Agilent Technologies (Santa Clara, CA, USA) SuperNova Single Source diffractometer with Mo$K\alpha$ ($\lambda$ = 0.71073 Å) (**2**), using the CrysAlis Pro software version 1.171.40.67a [28]. In all cases, the analytical numeric absorption correction using a multifaceted crystal model based on expressions derived by R.C. Clark and J.S. Reid was used [29]. The structural determination procedure was carried out using the SHELX package [30,31]. The structure was solved with the intrinsic phasing method, and a successive least-square refinement was then carried out based on the full-matrix least-squares method on $F^2$ using the SHELXL-2018/3 program [30,31]. All H-atoms were positioned geometrically, with the C–H equal to 0.93, 0.96, and 0.97 Å for the aromatic, methylene, and methyl H-atoms, respectively, and refined as fixed.

### *2.3. Computational Study*

#### 2.3.1. Quantum Chemical Studies

Starting from the X-ray structure of $(BTMA)_2[PtCl_6]$, the geometry of the $BTMA^+$ cation in the singlet ground spin state was optimized in vacuo and in aqueous solutions at the MP2 [32,33] level of theory using the cc-pVTZ basis set from the Gaussian library [34]. Solvent effects were accounted for using the SMD (solvent model based on density) [35] approximation. Stable structures were tested for the absence of imaginary vibrations using vibrational analysis. All quantum chemical calculations were performed using the Gaussian09 software, version 9.0 (Gaussian Inc.: Wallingford, CT, USA, 2011) [34]. Frontier molecular orbitals were drawn using the MOLEKEL software, version 5.4.0.8 (Swiss National Supercomputing Centre: Manno, Switzerland, 2009) [36] from the Gaussian09 output. The map of the electrostatic potential of $BTMA^+$ at the Hartree–Fock level of theory was drawn using the Avogadro software, version 1.98 [37].

The electronic structure in terms of the QTAIM (quantum theory of atoms-in-molecule) topological analysis of electron density is described as follows [38]. Atomic charges and volumes were obtained by integration of electron density and space over atomic basins (up to 0.001 a.u. isosurface), respectively. Bond critical points (BCPs) are saddle points of electron density on the bond paths between individual atom pairs. A set of bond paths is

denoted as a molecular graph. The BCP electron density, $\rho_{BCP}$, reflects the bond strength. Its Laplacian, $\nabla^2\rho_{BCP}$,

$$\nabla^2\rho_{BCP} = \lambda_1 + \lambda_2 + \lambda_3 \quad (1)$$

where $\lambda_1 < \lambda_2 < 0 < \lambda_3$ are the eigenvalues of the Hessian of the BCP electron density, which depicts the relative electron density contribution of the bonded atoms (negative values correspond to covalent bonds). The BCP bond ellipticity, $\varepsilon_{BCP}$,

$$\varepsilon_{BCP} = \lambda_1/\lambda_2 - 1 \quad (2)$$

describes the bond deviation from cylindrical symmetry (such as in ideal single or triple bonds) due to its double-bond character, mechanical strain, or other perturbations.

The electron delocalization index, DI, is the average number of electrons delocalized (shared) between atom pairs. It corresponds to a bond index if both atoms are connected by a bond path [39]. The QTAIM analysis was performed using the AIMAll software [39] from *.wfn files produced by the Gaussian09 software, version 9.0 (Gaussian Inc.: Wallingford, CT, USA, 2011). Molecular graphs were drawn using the AIM2000 software, version 1.0 [40]. The superposition of the optimized structures was optimized using the PyMol software, ver. 1.8 [41,42]. The root mean square deviations (RMSDs) of the corresponding atomic positions of individual pairs of structures were evaluated using the script (www.github.com).

#### 2.3.2. Hirshfeld Surface Analysis

The 3D Hirshfeld surfaces (HSs) and corresponding 2D fingerprint calculations were carried out in CrystalExplorer [43] based on the methods reported in the literature [44]. The maps of Hirshfeld's surfaces were prepared using $d_{norm}$, shape index, curvedness, and fragment patch propensity. Fingerprint plots show a qualitative description of close contacts in the crystals as a function of the $d_i$ and $d_e$ values [44].

#### 2.3.3. Enrichment Ratio

The enrichment ratios (ERs) of the intermolecular interactions observed in the crystal structures **1**–**4** were calculated based on the HS methodology [45] as the ratio between actual and random inter-contacts. In this context, privileged (with ER larger than unity) and disfavored (with ER smaller than unity) inter-contacts were described in the analyzed crystals.

#### 2.3.4. Energy Frameworks

The pairwise interaction energies between the moieties in the crystals were calculated using the CrystalExplorer 21.5 program [46] using the wave function calculated at the B3LYP/6-31G(d,p) functional basis set that is widely accepted in computational chemistry. More specifically, the electrostatic ($E_{ele}$), polarization ($E_{pol}$), dispersion ($E_{disp}$), and exchange repulsion ($E_{rep}$) energy components, according to the Equation presented below, were calculated [47].

$$E_{tot} = E_{ele} + E_{pol} + E_{disp} + E_{rep} \quad (3)$$

A molecular cluster with a radius of 3.8 Å was generated around a selected single moiety of the reference compound.

The total energy was calculated using scaling factors such as $K_{ele}$ = 1.057, $K_{pol}$ = 0.740, $K_{dis}$ = 0.871, and $K_{rep}$ = 0.618 [47,48].

#### 2.3.5. CSD-Materials Module

The Cambridge Crystallographic Data Centre Mercury 4.0 program (version 2024.3.1) [49], along with selected functionalities from the CSD-Materials module, was used in this study.

Before any calculations, the molecular structures were standardized according to the Cambridge Structural Database conventions for bond types, and default settings were applied for all subsequent calculations. To assess the preferred interaction behavior, full interaction maps (FIMs) were generated for the studied crystals based on CSD interaction data [50]. This approach allowed for the visualization of interaction landscapes using 3D coordinates obtained from X-ray crystallographic data. Calculations were performed using the Aromatic Analyser, a neural network-based tool that quantitatively evaluates aromatic ring interactions within crystal structures. Only interactions classified as strong (scores of 10–6) or moderate (scores of 4–6) on a 1–10 scale were considered. The topology of intermolecular connections in the analyzed series was assessed by representing each cation as a single point located at its center of gravity. Connections were established based on identified weak interactions. Anions were represented by the position of their heavy atom, and the charge-assisted C–H···Cl hydrogen bonds were depicted as linkers connecting the cations.

## 3. Results and Discussion

### *3.1. Crystallographic Study*

Crystals of **1–4** were successfully obtained, and their 3D structures were determined by the single-crystal X-ray diffraction method with high precision at low temperatures. The compounds **1**–**3** crystallize in the monoclinic centrosymmetric space groups (**1** in $P2_1/c$, 2 in $C2/c$, and 3 in $P2_1/n$), whereas the compound **4** crystallizes in the orthorhombic noncentrosymmetric space group $P2_12_12_1$. The asymmetric unit of the crystal lattice of **1** contains one benzyltrimethylammonium cation and half of the inorganic anion, while in **2,** one cation and two individual halves of an anion are present. The metal atoms of all the above anions lie on the symmetry elements. On the other hand, in the analyzed crystals of **3** and **4,** we are dealing with a situation where two benzyltrimethylammonium cations assist one inorganic anion, and all atoms of the latter have a general position.

As mentioned, all four analyzed salts contain benzyltrimethylammonium cations; however, differences in their intrinsic geometries are rather small. As can be seen in the figure showing the overlay of their structural skeletons, differences manifest as a slight rotation of the trimethylammonium moiety (Figure 1). The substantial distinctions among the individual salts manifest in their overall supramolecular architecture. The geometry around the Pt atom in the hexachloroplatinate anion (in **1**) is octahedral, while around the Cu atom in the tetrachlorocuprate (in **3**) and tetrabromocuprate (in **4**) anions it is slightly distorted and tetrahedral. Interestingly, in **1**, the hexachloroplatinate anion lies on the inversion center and two-fold axis.

The molecular structures of the analyzed salts are depicted in Figure 1. Complete crystal data and refinement details of the analyzed salts are collected in Table 1. The datasets have been deposited in the Cambridge Crystallographic Data Centre under CCDC numbers 2464968–2464971. Selected bond lengths and angles of **1–4** are summarized in Tables S1–S12 in the Supplementary Materials Section. The values are similar to those found in the literature.

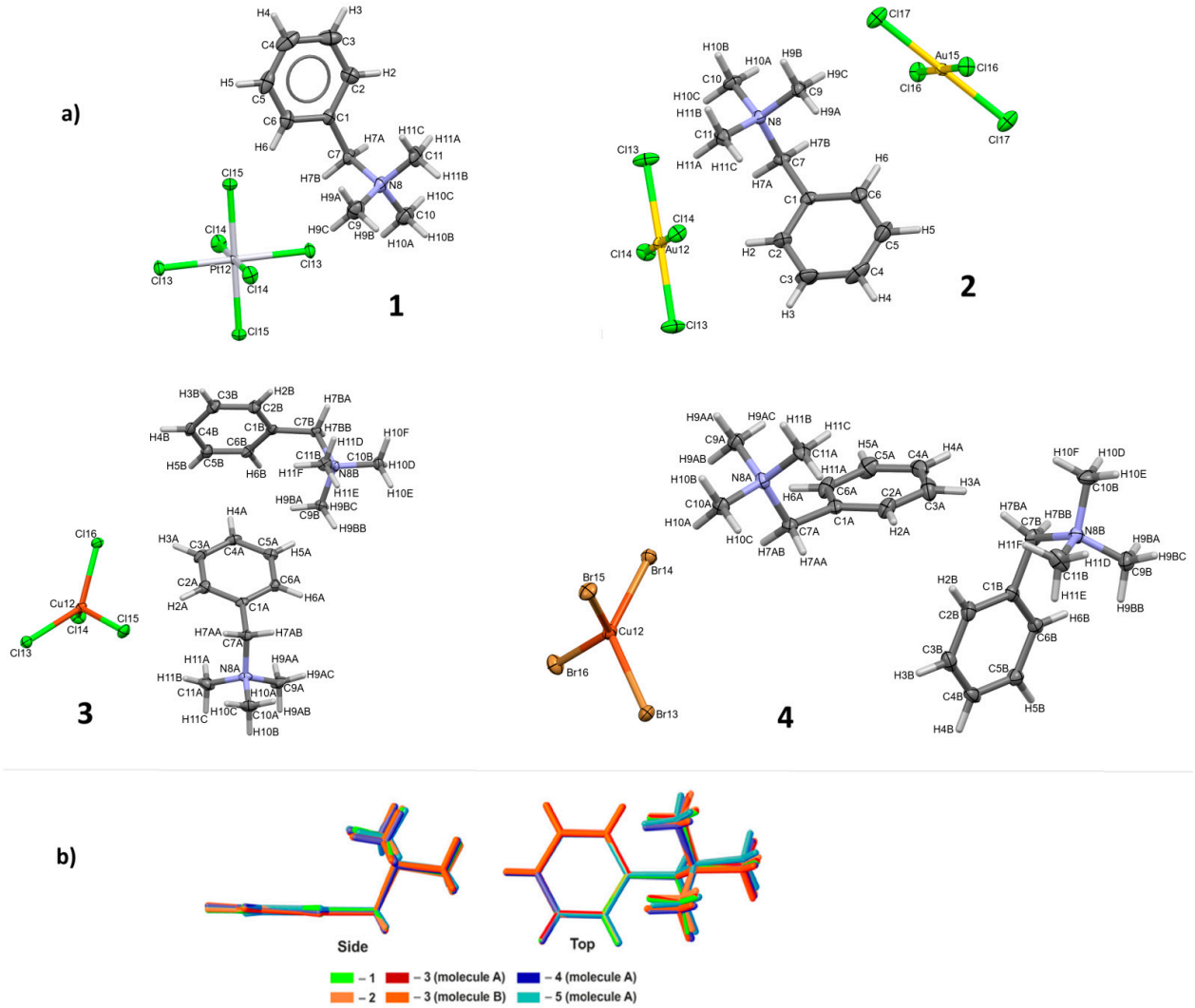


**Figure 1.** (**a**) Molecular structures of **1**–**4** showing the atom numbering scheme. (**b**) Overlay of the structural skeletons of the benzyltrimethylammonium moieties in the crystals of **1**–**4**.

**Table 1.** Crystal data and refinement details of **1**–**4**.

| **Compound** | **1** | **2** | **3** | **4** |
|---|---|---|---|---|
| Empirical formula | $C_{20}H_{32}Cl_6N_2Pt$ | $C_{10}H_{16}AuCl_4N$ | $C_{20}H_{32}Cl_4CuN_2$ | $C_{20}H_{32}Br_4CuN_2$ |
| Formula weight | 708.26 | 489.00 | 505.81 | 683.65 |
| Temperature/K | 100(2) | 100(2) | 100(2) | 100(2) |
| Crystal system | monoclinic | monoclinic | monoclinic | orthorhombic |
| Space group | $P2_1/c$ | $C2/c$ | $P2_1/n$ | $P2_12_12_1$ |
| $a$/Å | 10.9703(2) | 16.7055(3) | 9.49010(16) | 9.1205(2) |
| $b$/Å | 11.9807(3) | 14.3876(2) | 9.02423(19) | 9.6086(3) |
| $c$/Å | 9.6767(2) | 13.9779(2) | 27.9964(4) | 28.8970(7) |
| $\alpha$/° | 90 | 90 | 90 | 90 |
| $\beta$/° | 91.7727(19) | 114.613(2) | 92.1082(14) | 90 |
| $\gamma$/° | 90 | 90 | 90 | 90 |
| Volume/Å$^3$ | 1271.22(5) | 3054.37(9) | 2396.01(8) | 2532.38(11) |
| $Z$ | 2 | 8 | 4 | 4 |
| $\rho_{calc}$g/cm$^3$ | 1.850 | 2.127 | 1.402 | 1.793 |
| $\mu$/mm$^{-1}$ | 16.206 | 10.308 | 5.442 | 8.661 |
| $F(000)$ | 692.0 | 1840.0 | 1052.0 | 1340.0 |
| Crystal size/mm$^3$ | 0.39 × 0.06 × 0.05 | 0.18 × 0.09 × 0.04 | 0.24 × 0.17 × 0.08 | 0.36 × 0.28 × 0.06 |
| Radiation | Cu$K\alpha$ ($\lambda$ = 1.54184) | Mo$K\alpha$ ($\lambda$ = 0.71073) | Cu$K\alpha$ ($\lambda$ = 1.54184) | Cu$K\alpha$ ($\lambda$ = 1.54184) |
| 2Θ range for data collection/° | 8.064 to 136.446 | 4.28 to 52.744 | 6.318 to 134.158 | 6.118 to 134.138 |
| Index ranges | $-13 \le h \le 13$, $-14 \le k \le 13$, $-11 \le l \le 11$ | $-20 \le h \le 20$, $-17 \le k \le 17$, $-17 \le l \le 17$ | $-9 \le h \le 11$, $-10 \le k \le 10$, $-33 \le l \le 32$ | $-10 \le h \le 8$, $-11 \le k \le 11$, $-30 \le l \le 34$ |
| Reflections collected | 18,563 | 30,718 | 24,060 | 8980 |

**Table 1.** *Cont.*

| Compound | 1 | 2 | 3 | 4 |
|---|---|---|---|---|
| Independent reflections | 2327 [$R_{int}$ = 0.0414, $R_{sigma}$ = 0.0185] | 3126 [$R_{int}$ = 0.0305, $R_{sigma}$ = 0.0149] | 4294 [$R_{int}$ = 0.0305, $R_{sigma}$ = 0.0194] | 4524 [$R_{int}$ = 0.0271, $R_{sigma}$ = 0.0313] |
| Data/restraints/parameters | 2327/0/136 | 3126/0/150 | 4294/0/250 | 4524/0/250 |
| Goodness-of-fit on $F^2$ | 1.072 | 1.069 | 1.202 | 1.049 |
| Final $R$ indexes [$I \geq 2\sigma$ ($I$)] | $R_1$ = 0.0203, $wR_2$ = 0.0466 | $R_1$ = 0.0120, $wR_2$ = 0.0250 | $R_1$ = 0.0361, $wR_2$ = 0.0873 | $R_1$ = 0.0226, $wR_2$ = 0.0562 |
| Final $R$ indexes [all data] | $R_1$ = 0.0223, $wR_2$ = 0.0481 | $R_1$ = 0.0145, $wR_2$ = 0.0257 | $R_1$ = 0.0388, $wR_2$ = 0.0884 | $R_1$ = 0.0240, $wR_2$ = 0.0567 |
| Largest diff. peak/hole/e Å$^{-3}$ | 1.65/−0.92 | 0.61/−0.35 | 0.56/−0.45 | 0.31/−0.51 |

### 3.2. Supramolecular Features of **1**–**4**

The full interaction maps (FIMs) for **1**–**4** that were calculated based on statistical information on interactions derived from the CSD [50] are presented in Figure 2. They helped to check the preferred interaction behavior and understand the effect of different anions on the formation of supramolecular synthons. Overall, the dark zones indicate a high tendency for synthon formation. The predicted most-likely positions of functional groups with a crystal packing indicated that corresponding crystals fulfill the expected H-bonding and π-based interactions. First of all, a thorough comparative analysis indicated a lack of classical interactions in all the analyzed structures since blue and red zones for the H-bonding donor and acceptor probabilities are absent. Moreover, nearly identical beige–brown landscapes of aromatic–hydrophobic interactions were obtained. Notably, subtle but essential differences are visible. The color intensity of the regions correlates with the likelihood of the corresponding interactions. The functional groups have slightly different probabilities of being involved in aromatic–hydrophobic (beige–brown areas) and non-classical H-bonding (claret areas) interactions. The generated synthons by the latter interactions are discussed in the section below. Moving forward, the specificity of the studied salts resulted from the restricted functional groups and low availability of H-atom acceptors; hence, the crystal packing in all supramolecular systems is driven only by non-classical intermolecular interactions, such as C–H···Cl and C–H···Br (in **4**). The donor-to-acceptor distances vary from 3.563 Å for C–H···Cl in **1** to 3.838 Å for C–H···Br in **4**. Thus, the supramolecular networks of the investigated compounds are governed via the presence of the anions containing the chlorine and bromine atoms as H-acceptors of hydrogen bonds. On the other hand, significant π···π interconnects are observed in **2** and, additionally, Cu–Br···π interconnects are observed in **4**. The geometric parameters associated with H-bonding interactions in compounds **1**–**4** are summarized in Table 2, while π-based interconnects are listed in Table S13. A detailed analysis using the Aromatic Analyser module is presented below.

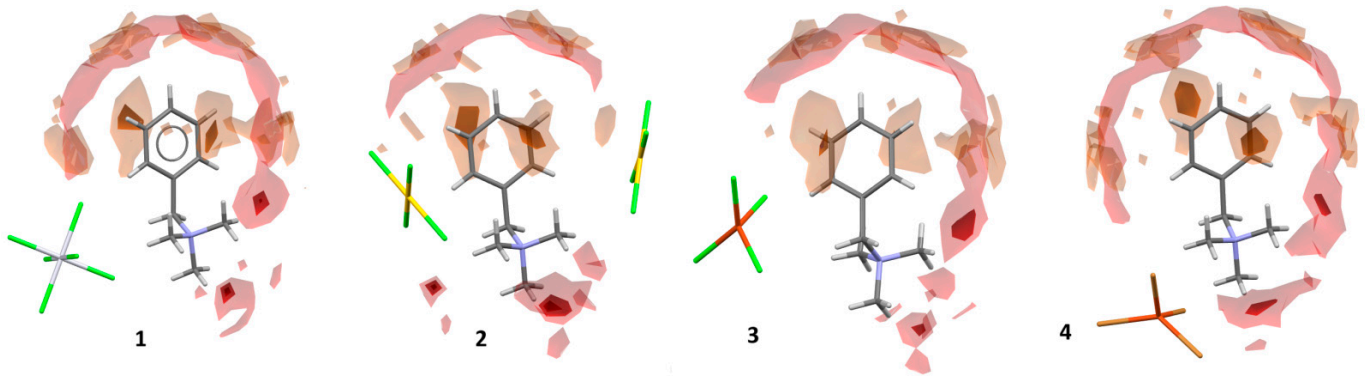


**Figure 2.** The 3D full interaction maps of **1**–**4**, with the possible areas of weak acceptors in dark red.

**Table 2.** Geometric parameters of H-bonds for **1**–**4**.

| D-H···A | D-H [Å] | H···A [Å] | D···A [Å] | H···A [º] |
|---|---|---|---|---|
| **1** | | | | |
| C7-H7A···Cl15 [i] | 0.97 | 2.63 | 3.563(4) | 162 |
| C10-H10A···Cl13 | 0.96 | 2.76 | 3.655(4) | 155 |
| Symmetry code: (i) x, 3/2-y, ½ + z | | | | |
| **2** | | | | |
| C7-H7A···Cl16 [i] | 0.97 | 2.82 | 3.701(2) | 152 |
| (i) 3/2-x, −1/2 + y, 3/2-z | | | | |
| **3** | | | | |
| C4A-H4A···Cl15 [i] | 0.93 | 2.77 | 3.615(3) | 152 |
| C7B-H7BB···Cl13 [ii] | 0.97 | 2.83 | 3.724(3) | 154 |
| C9B-H9BB···Cl16 [iii] | 0.96 | 2.82 | 3.688(3) | 151 |
| C11B-H11D···Cl16 [iv] | 0.96 | 2.75 | 3.646(3) | 155 |
| C11B-H11E···Cl16 [iii] | 0.96 | 2.77 | 3.654(3) | 153 |
| Symmetry codes: (i) x, −1 + y, z; (ii) 1 + x, −1 + y, z; (iii) 1 + x, y, z; (iv) 3/2-x, −1/2 + y, ½-z | | | | |
| **4** | | | | |
| C9A-H9AA···Br13 [i] | 0.96 | 2.92 | 3.802(5) | 153 |
| C4B-H4B···Br15 [ii] | 0.93 | 2.86 | 3.693(5) | 149 |
| C11A-H11A···Br13 [iii] | 0.96 | 2.89 | 3.786(5) | 155 |
| C11B-H11D···Br14 [iv] | 0.96 | 2.91 | 3.838(5) | 164 |
| Symmetry codes: (i) −1 + x, y, z; (ii) ½ + x, ½-y, 1-z; (iii) −1/2 + x, ½-y, 1-z; (iv) ½-x, 1-y, ½ + z | | | | |

The results of the calculations performed using the Aromatic Analyser module, integrated into the CSD Mercury 2024.3 software (CCDC, Cambridge, UK), are presented in Table S14. For compound **1**, only moderate C–H···π interactions (score 5.8) were observed. In contrast, compound **2** exhibited strong π···π interactions (score 8.9), characterized by a parallel orientation of the rings with a centroid distance of 3.932(2) Å. Additionally, moderate off-set stacking interactions (score 5.3) were detected. In structure **3**, both cations are only weakly connected. The highest score of 4.3 corresponds to C–H···π interactions between crystallographically different cations. Similar interactions were found in compound **4**, with a maximum score of 4.5.

The crystal packing of the studied structures is illustrated in Figures 3–6, showing, at first glance, different supramolecular architectures. The crystals of the salts differ by networks of non-covalent (supramolecular) interactions and stacking modes. Nevertheless, a thorough examination revealed a high similarity of the topology of packing in **3** and **4** crystals and a lower similarity between **1** and **2** crystals. In **1** and **2**, benzyltrimethylammonium cations are arranged in an antiparallel fashion bonded by the hexachloroplatinate and tetrachloroaurate anions, respectively, giving rise to a layer-like structure with the alternation of two sub-layers of apolar cations and polar anions prolongated along the crystallographic axis *b*. Nevertheless, in **2**, the different positions of anions adopt different twisted (about 90°) arrangements relative to each other. Notably, in **1**, the octahedral anion participates in bi- and tetrafurcated hydrogen bonds. The crystal packing of **3** and **4** is very similar. Benzyltrimethylammonium cations are arranged in a head-to-tail fashion and connected via tetrachlorocuprate and tetrabromocuprate anions, respectively. Consequently, 'twisted' cationic sub-layers are observed. Both in **3** and **4**, distorted tetrahedral anions participate in multi-furcated hydrogen bonds.

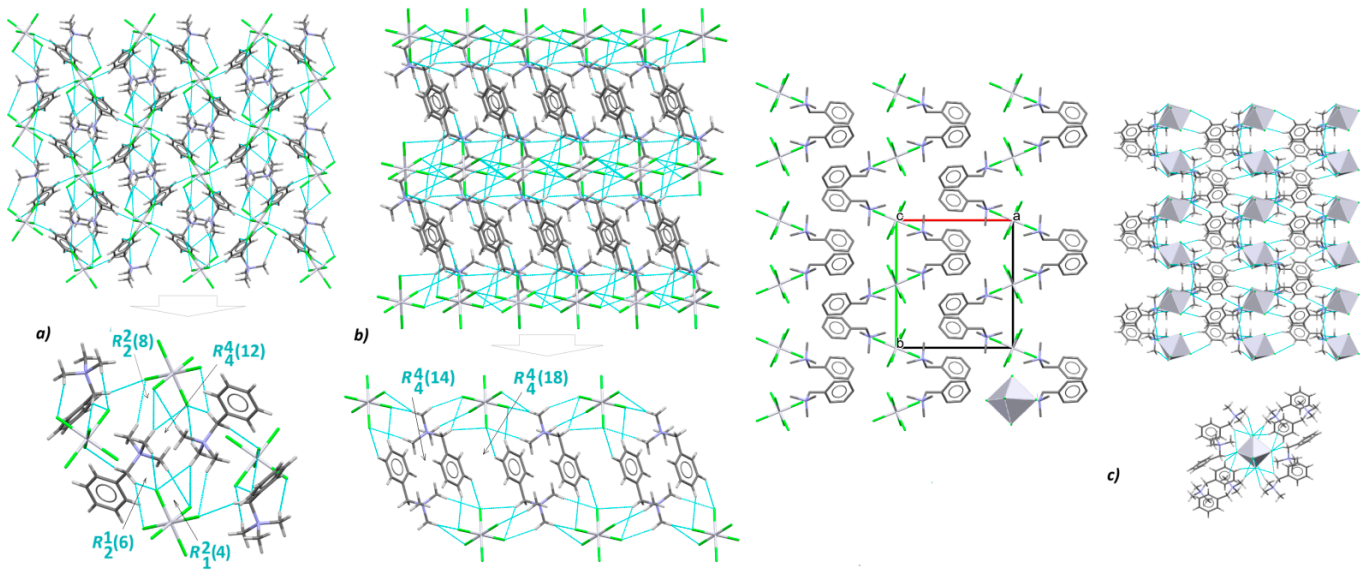


**Figure 3.** Crystal packing of **1** along the (**a**) (on the left), (**b**) (middle), and (**c**) (on the right) crystallographic axes.

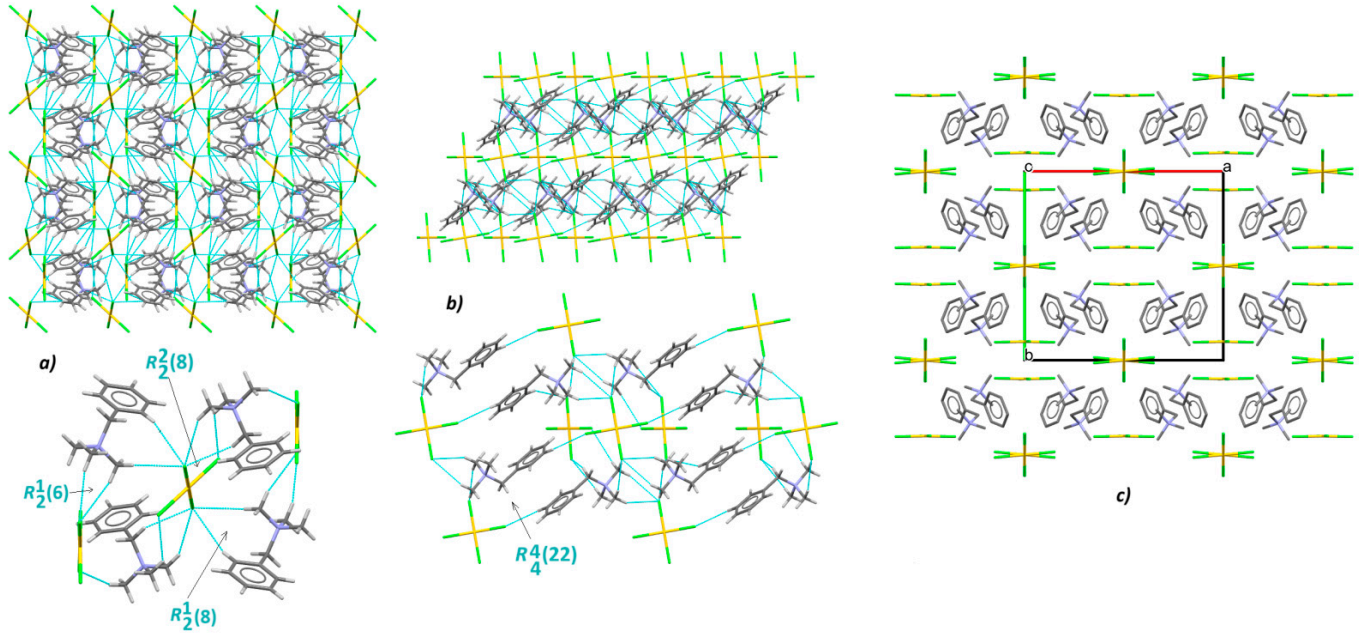


**Figure 4.** Crystal packing of **2** along the (**a**) (on the left), (**b**) (middle), and (**c**) (on the right) crystallographic axes.

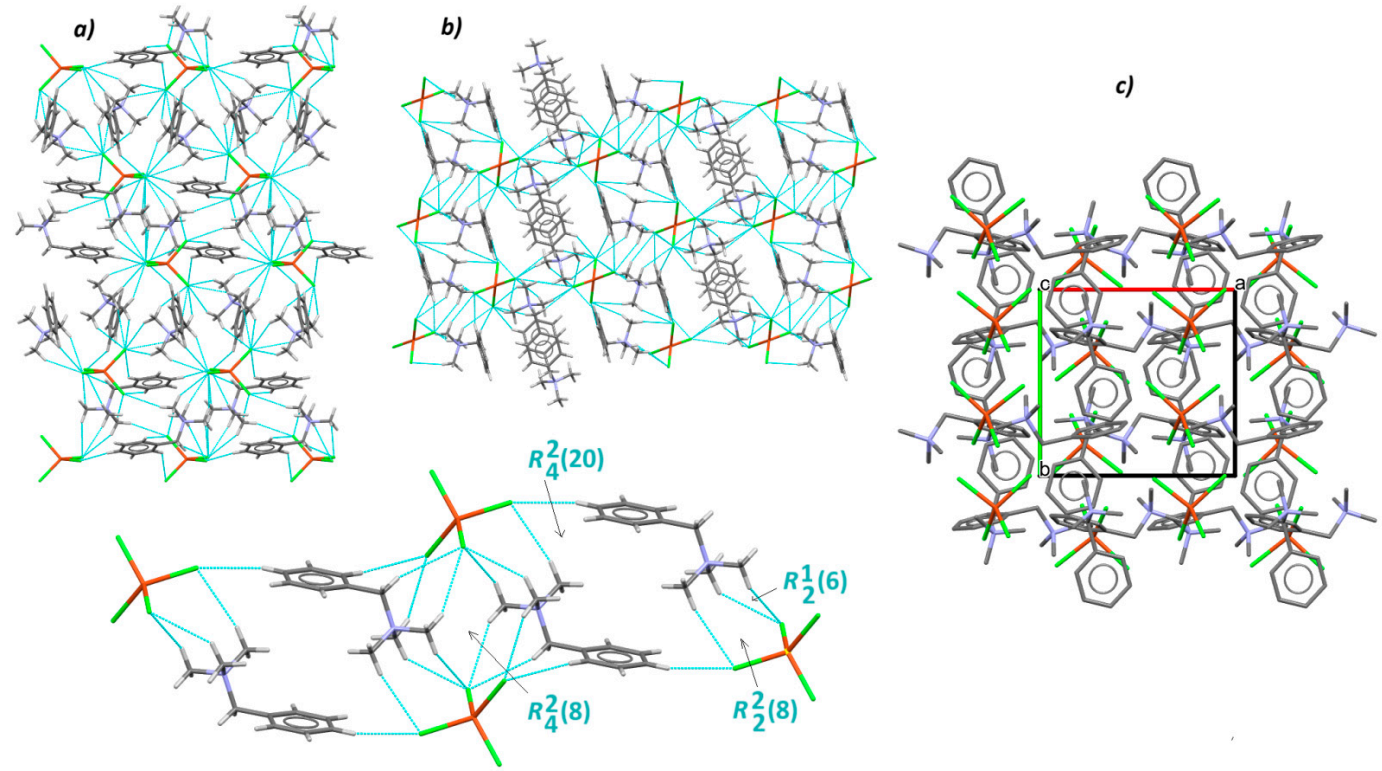


**Figure 5.** Crystal packing of **3** along the (**a**) (on the left), (**b**) (middle), and (**c**) (on the right) crystallographic axes.

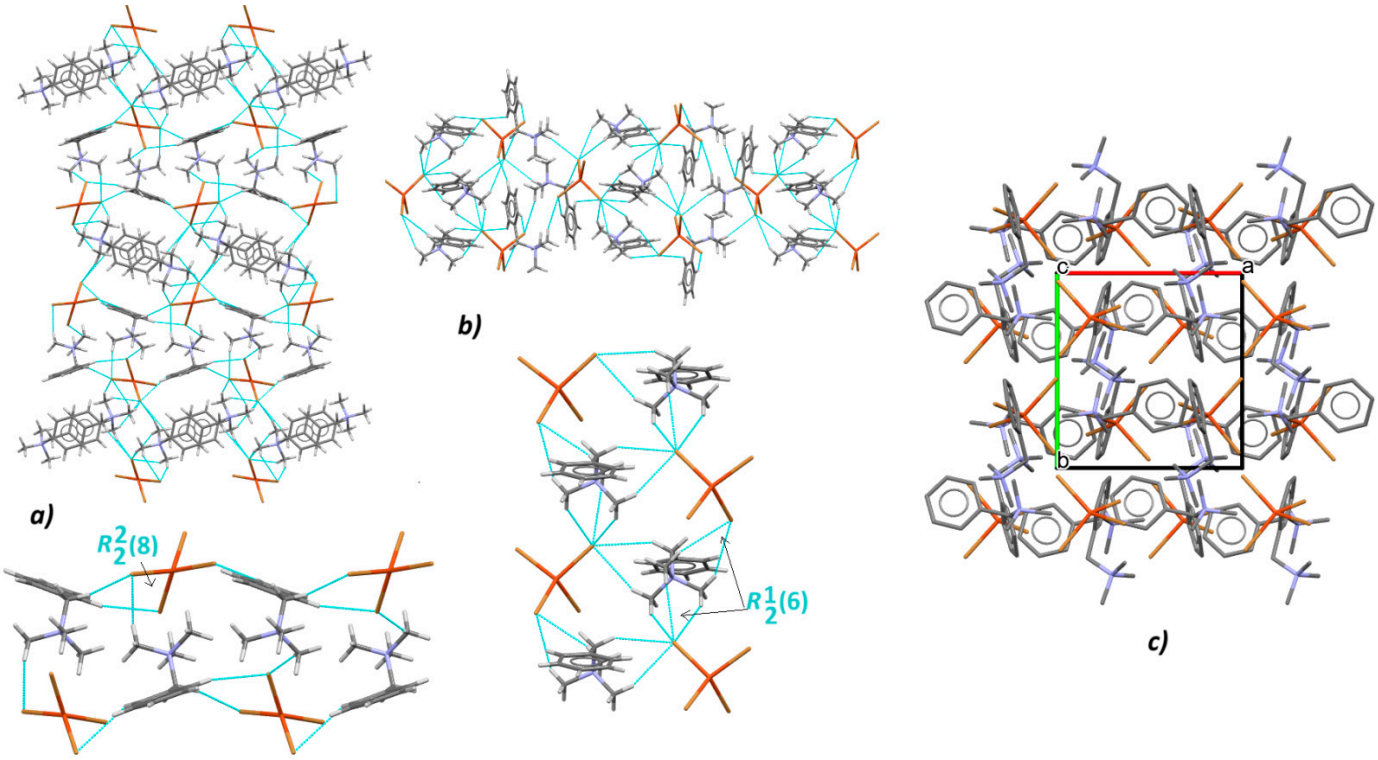


**Figure 6.** Crystal packing of **4** along the (**a**) (on the left), (**b**) (middle), and (**c**) (on the right) crystallographic axes.

In all the analyzed crystals, the ions are linked together by C–H···Cl (in **1**–**3**) and C–H···Br (in **4**), respectively, enclosing diverse dimers (*D*) at the first level of the graph set

theory, and chains (*C*) and rings (*R*) at the second level of the graph set theory, according to Etter's rules [51,52]. Additionally, in **2**–**4**, *D* motifs are also constructed at the second level. Thus, only two types of non-classical interactions resulted in a rich portfolio of supramolecular H-bonding motifs (Table S15). It can be observed that the benzyltrimethylammonium cation may be considered as a supramolecular tecton engaging in the building of synthonic recurring cyclic motifs in all the analyzed crystals. Only heterosynthons are generated, by different functional groups, in all supramolecular systems. All cyclic intermolecular synthons (*R*) are formed only between cations and anions.

More importantly, supramolecular interchangeable/equivalent synthons are observed (Figure 7 and Figure S1). They may be helpful in the design of similar compounds with controllable properties. Among them, bifurcated synthons are dominant. It should be noted that some of the robust synthons are stabilized by π···π (in **2**) and Cu–Br···π (in **4**) (Figure 7) interactions. It is worth mentioning that the $R^1_2(6)$ bifurcated synthon is present in all four crystal structures.

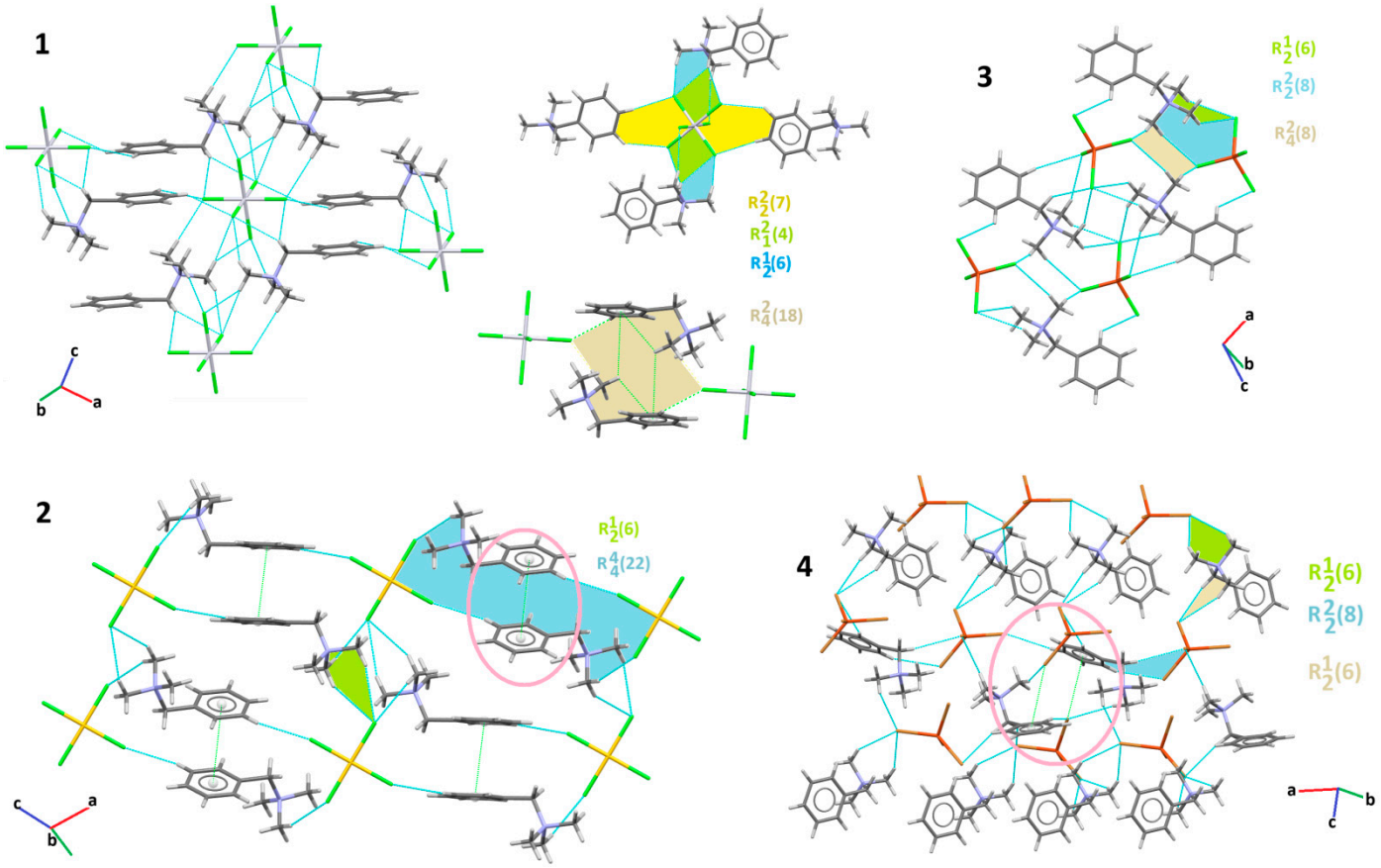


**Figure 7.** Fragments of the supramolecular architectures of **1**–**4** showing the intermolecular interactions between neighboring moieties and recurring H-bonding motifs that are stabilized by π···π interactions in **2** and Cu–Br···π interactions in **4** (pink circles).

Taking into account the aromatic interactions between cations and the C–H···Cl contacts between differently charged entities, the topology of the resulting supramolecular networks was analyzed. In Figure 8, the cations are reduced to a node (black balls), representing the center of gravity of each moiety. In compounds **3** and **4**, two crystallographically independent cations are shown in white and black, respectively. In **1**, the cations are linked via two C–H···π interactions between aromatic rings, with one of the $CH_3$ groups acting as a weak donor. These two interactions operate between the same pair of cations, resulting in the formation of a chain of cations propagating along the shortest unit cell axis c. Two

detected cation–anion hydrogen bonds of the C–H···Cl type link these chains into an undulated layer perpendicular to the [100] direction. The topology descriptor of the layer can be given as 4(3·2.6) + 4(3·2.6) and its symmetry is in accordance with the p21/b layer symmetry group.

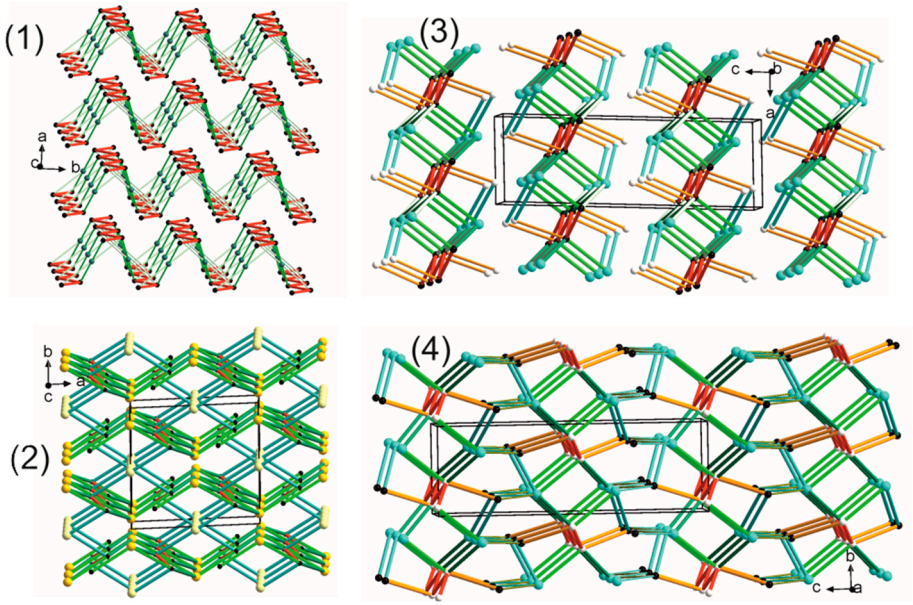


**Figure 8.** Topological representation of intermolecular interactions in the **1**–**4** crystals. The black and white balls represent the centers of gravity of the cations. The anion is reduced to the position of the heavy metal only. The red and orange lines represent C–H···π and π···π interactions between cations. Links are shown in green, and cyan shades are in line with the C–H···Cl(Br) hydrogen bonds. In **4**, the brownish line represents Br···π interactions.

The main interaction occurring between cations in **2** is π···π stacking, which topologically leads to the formation of a dimer. The two independent anions bind weakly to the cations via C–H···Cl interactions, resulting directly in the formation of a three-dimensional (3D) structure. It should be noted that the topological environment of these two anions is different (LK = 2 and LK = 4), which further complicates the description of this network. However, it can be seen that one of the anions (LK = 4) and the cation form infinite chains along the [10-1] direction with a 4(3·2) + 4(3·2) topology and the p2/c rod symmetry group. Through the second anion (vertex with LK = 2), they combine into a 3D structure. In **3**, there are two crystallographically independent cations, denoted by white and black balls, respectively. Weak aromatic interactions join two different cations, forming a dimeric, finite motif, whereas relatively short $CH_3$···π contacts are observed between cations labeled as B (black balls). The connections visible in Figure 8 are denoted with red and orange lines, topologically representing a decorated chain along the [010] direction. Together with the observed C–H···Cl hydrogen bonds (see Table S15, shown as green shaded lines in Figure 8), the resulting topology forms a layer perpendicular to the longest unit cell vector c. The topological descriptor can be given as $4(4{\cdot}4.6_2.4) + 5(4{\cdot}5) + 2(4)$ and the symmetry of the layer group is p21/b. Similarly to salt **3**, in **4**, two independent cations are connected via weak aromatic interactions, forming a decorated chain propagating along the [100] direction. However, more numerous C–H···Br hydrogen bonds, as well as detected Br···π interactions, link the supramolecular cationic chains directly into a three-dimensional (3D) structure. In this case, the topology can be described using the same layer descriptors as in structure **3**, and only the linkers between the metal vertex and the cation are taken into account, marked as a black sphere.

Interestingly, the crystal structure similarity calculations (performed using Mercury) revealed that, in the crystals of **3** and **4**, 13 out of 15 molecules are identically oriented (see Figure S2; the mismatched molecule is denoted with a circle).

### *3.3. Hirshfeld Surface Analysis*

A Hirshfeld surface (HS) extended analysis was performed to obtain a deeper insight into the hierarchical preferences of close non-covalent interactions in the supramolecular assemblies of **1**–**4**. HS analysis is a valuable advancement that enables crystal engineers, including supramolecular chemists, to understand crystal packing behavior and design desired hierarchically ordered structures, thereby modulating their properties. HS maps were generated using not only a standard surface solution of $d_{norm}$ surfaces but also shape index, curvedness, and fragment patch surfaces (Figure 9). The Au-containing structure (**2**) was not included in the Hirshfeld surface and energy framework analyses owing to limitations of CrystalExplorer in treating such heavy atoms.

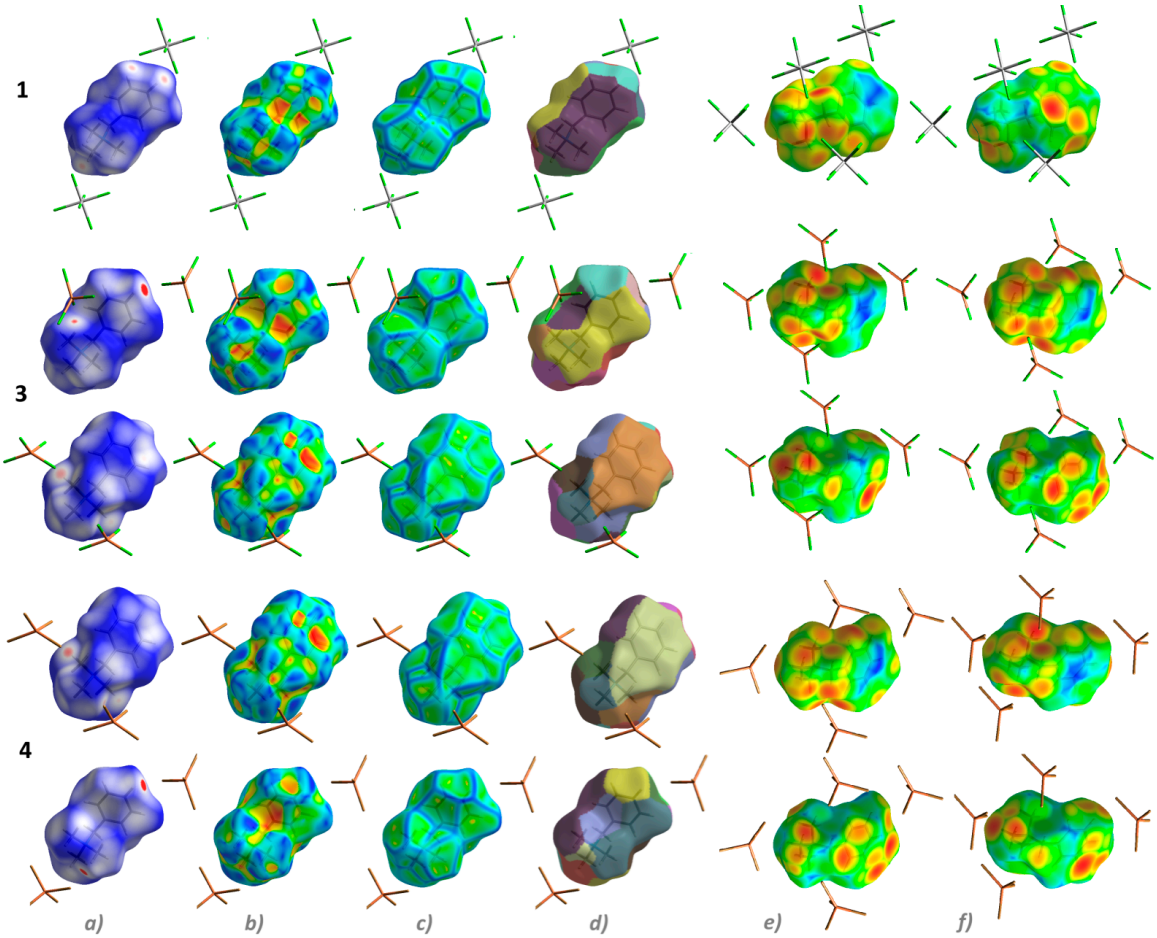


**Figure 9.** Comparison of Hirshfeld surface maps for cations in **1**,**3** and **4**: (**a**) $d_{norm}$, (**b**) shape index, (**c**) curvedness, (**d**) fragment patches, (**e**) $d_i$, and (**f**) $d_e$.

The surfaces were calculated for the cation, which is identical in all crystals, to identify differences in different environments. It should be noted that the red spots on the domain surfaces signify strong interactions, white indicates moderate interactions, while blue indicates negligible interactions. A thorough analysis of the maps revealed that the red regions are predominantly localized around the methyl groups (and also the phenyl groups) of the cations, signifying that this is a primary hydrogen-bonding site involved in intermolecular interactions. The surfaces are indicative of non-classical hydrogen-bonding

contacts, representing interactions with symmetry-related anions. More specifically, the small red spots on the maps of the $d_{norm}$ surfaces characterize closer distances than the van der Waals radii; here, H-bonding interactions such as C–H···Cl(Br) can be observed. To further investigate the similarities and differences in the weak interactions among the analyzed crystals, color maps of additional Hirshfeld surface properties were generated. Alternating red and blue areas indicate different weak interactions connecting cations with anions. Poorly visible adjacent red and blue triangles on the shape index surfaces, as well as poorly outlined flat green regions on the curvedness maps, indicate a lack of significant π-based interactions in the analyzed crystals. However, yellow–orange deformations in **4** may reveal Cu–Br···π interconnects. The colored fragment patches may indicate the number of nearest surrounding moieties that interact with the cation.

According to the commonly accepted criteria in Hirshfeld surface analysis, only contacts contributing more than 0.9% to the Hirshfeld surface are considered statistically meaningful for interpretation. In the studied structures, the Cu···H/H···Cu and Cl···H/H···Cl contacts exceed this threshold (1.5–1.6%), which allows their reliable quantitative evaluation. Their enrichment ratios ($E \geq 1$) further indicate that these interactions are statistically favored, although not dominant, within the crystal packing.

Fingerprint plots summarizing the intricate information are unique for each crystal. Nevertheless, the calculated fingerprint diagrams for **1**–**4** are very similar. They are characteristic of strong non-classical interactions due to a lack of inter alia long spikes (specific for O···H/H···O hydrogen bonds) on the histograms. The H···H contacts are observed in the middle area between the short spikes of Cl···H/H···Cl (in **1** and **3**) and Br···H/H···Br (in **4**), while the C···H/H···C interactions are visualized as 'wings' in the upper side of fingerprint plots of all crystals (Figure 10). H···H interactions are the largest contributors to the total crystal packing (from 55.2% in 1 to 61.7% in 3), while C···H/H···C interactions are the next most significant contributors, representing from 9.5% in **3** to ~19% in **1**. Cl···H/H···Cl (in **1** and **3**) and Br···H/H···Br (in **4**) are additional contributors, at the 25.5% level. Furthermore, Cu···H/H···Cu (~1.6%) in **3** and **4**, and C···Br/Br···C in **4** (1.5%) are also present. Notably, C···C interactions represent only a small fraction in **3** and **4** (below 1%). The percentage contribution of close contacts in these crystal structures is depicted in Figure 10. When considering the entire salts, halogen bonds Cl···Cl and Cl···Pt/Pt···Cl in 1 (~5%) are additionally observed (Figure S3). The enrichment ratio calculations based on Hirshfeld surface analysis indicate the propensity for specific intercontacts. Only contacts contributing more than 0.9% to the Hirshfeld surface are considered statistically meaningful [44]. In our structures, Cu···H/H···Cu and Cl···H/H···Cl contacts exceed this threshold (1.5–1.6%), allowing a reliable evaluation of their enrichment ratios. The calculated ratios ($E \geq 1$) show that these interactions are statistically favored, although not dominant, in the crystal packing. Similarly, Br···H/H···Br and Br···C/C···Br interactions in **4** are also favored. C···H/H···C interactions contribute prominently to all analyzed crystals. Notably, H···H contacts are always disfavored in the crystal packing despite their high contribution to the HSs in all structures (Tables S16–S20). In the context of halogen bonds such as Cl···Cl, these interactions do not play a significant role in the crystal packing.

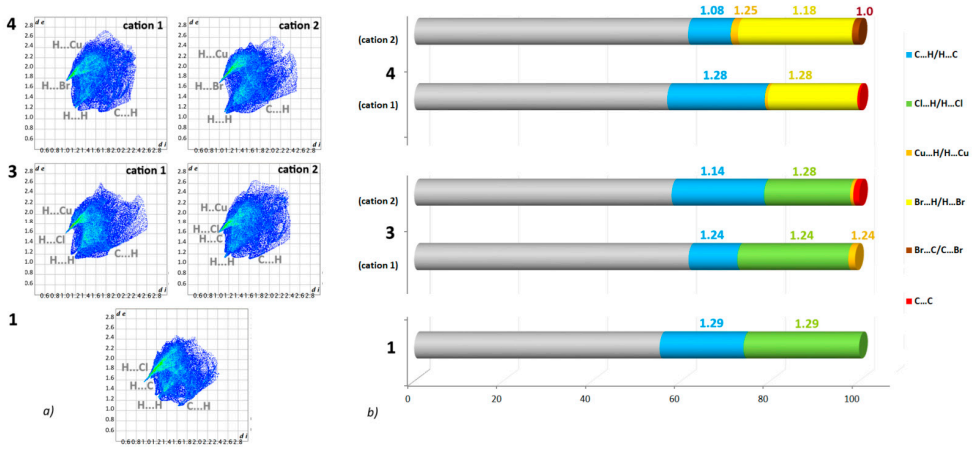


**Figure 10.** (**a**) Fingerprint plots for the overall interactions for **1**,**3** and **4** (**b**) Percentage contributions of inter-contacts in crystals **1**,**3** and **4** (above 1%). The enrichment ratio values are signified in the diagram by the same colors as their corresponding interactions.

### *3.4. Energy Frameworks*

The energy framework concept is helpful in either interpreting or visualizing the pairwise interaction energy between the neighboring moieties in the crystal. The 3D energy frameworks for the analyzed crystals, emphasizing the neighboring moieties in a radius of 3.8 Å from the central moiety, were calculated for the investigated salts. Energy types such as coulombic (red) and dispersion (green) are illustrated in Figures 11–15. It should be mentioned that the strength of interactions correlates with the size of the cylinders. The details, such as the crystallographic symmetry operations and their corresponding molecular energy values, which are crucial for calculating lattice energy [53] are summarized in Figures S4–S6. Salts **1** and **4** may be considered to be the most stable thermodynamically. It is noteworthy that the dispersion term is the significantly dominant component in all the analyzed crystals (Table S21), meaning that van der Waals forces have relevance.

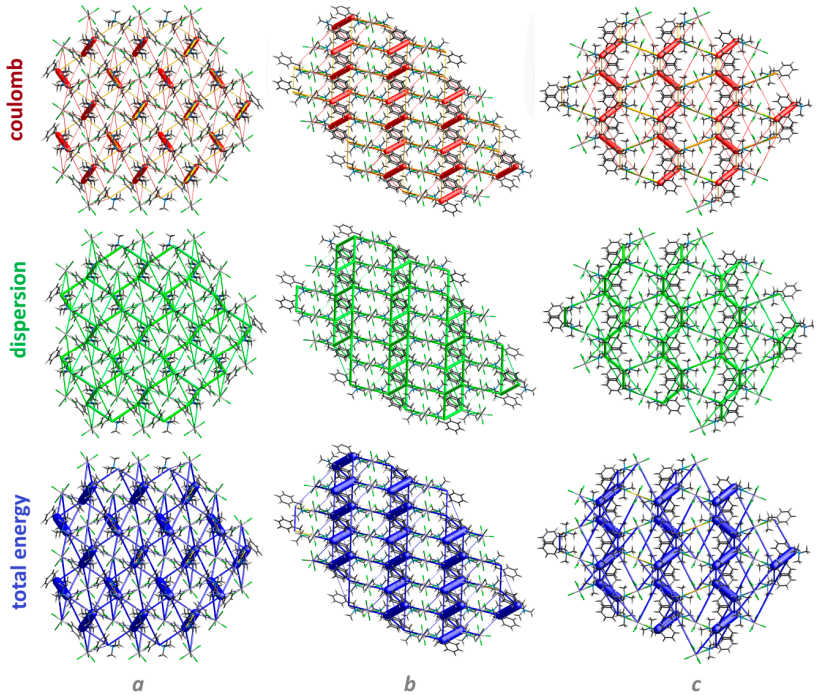


**Figure 11.** Energy framework plots for cations in **1**, showing the electrostatic and dispersion terms along a, b, and, c crystallographic axes, as well as the total energy interactions (the tube size is set to 100).

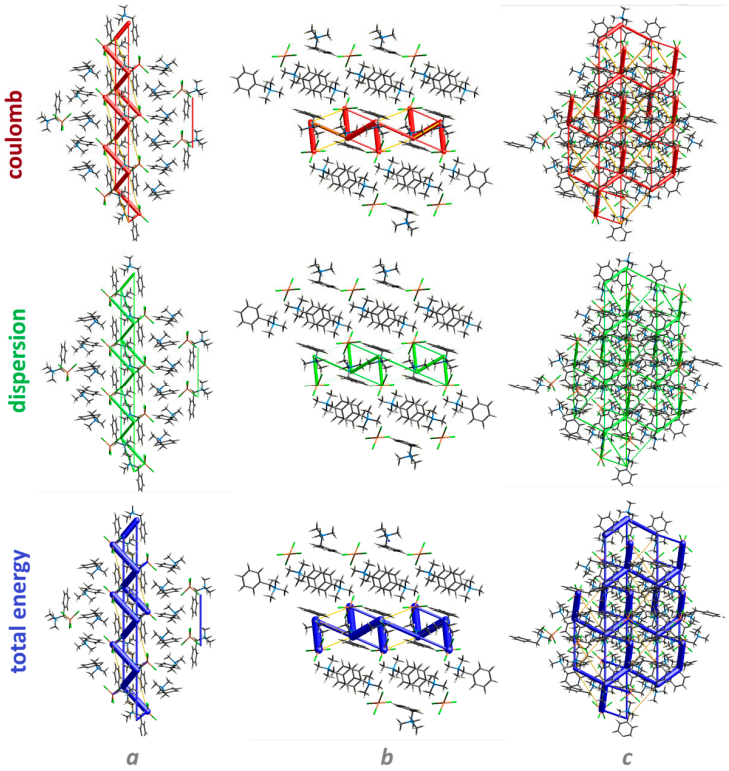


**Figure 12.** Energy framework plots for cation no. 1 in **3**, showing the electrostatic and dispersion terms as well as the total energy interactions (the tube size is set to 100).

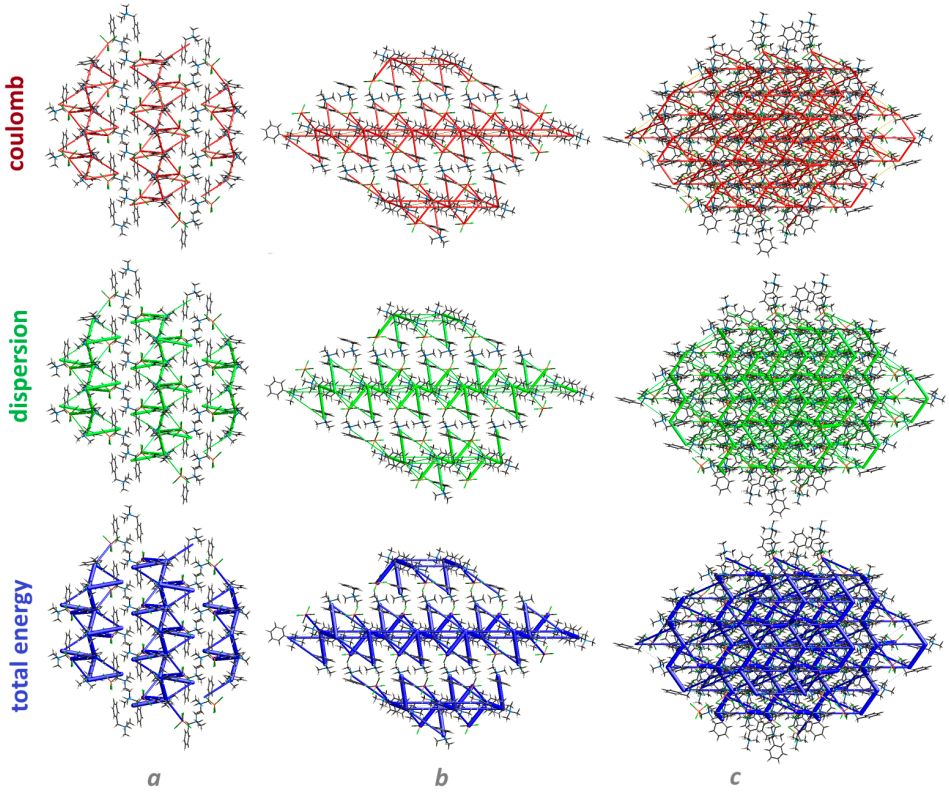


**Figure 13.** Energy framework plots for cation no. 2 in **3**, showing the electrostatic and dispersion terms as well as the total energy interactions (the tube size is set to 100).

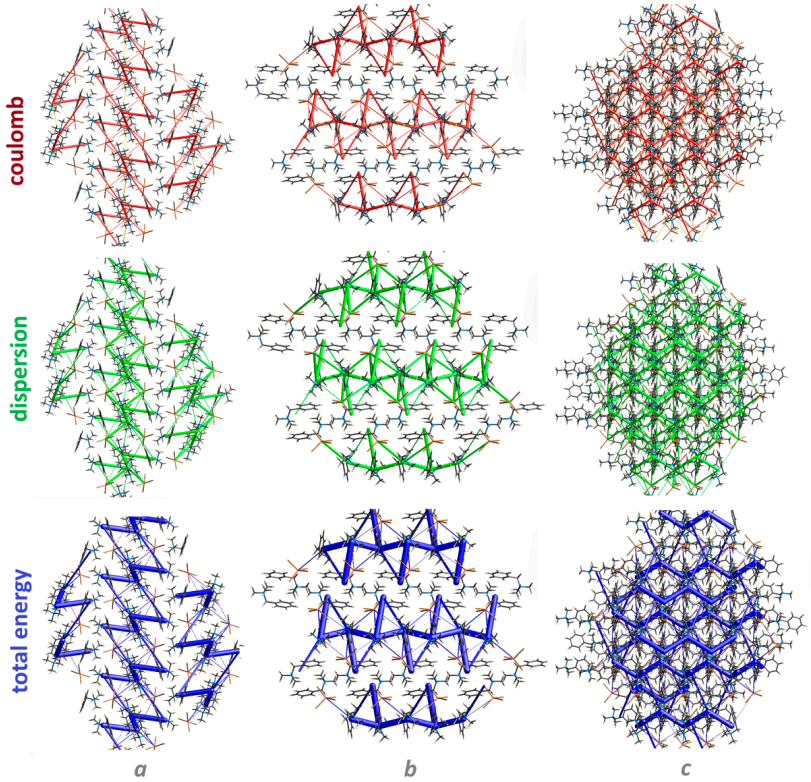


**Figure 14.** Energy framework plots for cation no. 1 in **4**, showing the electrostatic and dispersion terms as well as the total energy interactions (the tube size is set to 100).

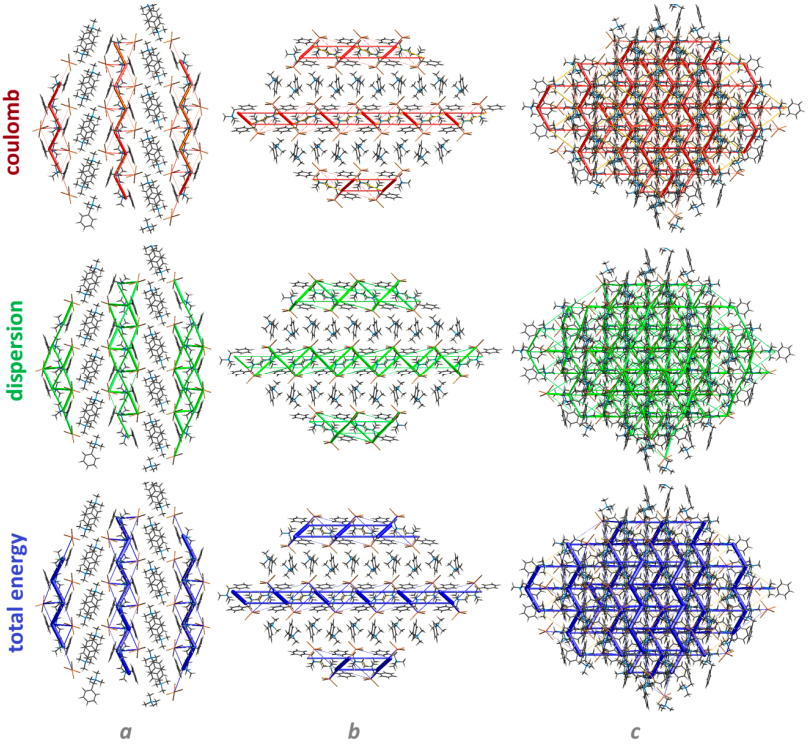


**Figure 15.** Energy framework plots for cation no. 2 in **4**, showing the electrostatic and dispersion terms as well as the total energy interactions (the tube size is set to 100).

### *3.5. Quantum Chemical Study*

The relevant structural parameters of the X-ray structures under study and of the MP2-optimized structure of $BTMA^+$ in aqueous solutions are presented in Table 3. As

expected, the largest differences are observed for the torsion angles. The X-ray $BTMA^+$ structures are affected by environmental influences, and so they lost their mirror plane. The symmetry group $C_s$ is preserved in the MP2-optimized structures. Another problem with the X-ray structures is the location of the H-atoms. The C–H bond lengths are fixed at 0.92–0.96 Å, whereas the MP2 optimizations produce the value of 1.08–1.09 Å, which should be closer to reality. In general, the differences between the X-ray structures of $BTMA^+$ in Table 3 are comparable with the differences between them and the MP2-optimized ones.

**Table 3.** Relevant bond lengths, bond angles, and dihedral angles in the compounds under study (see Figure 1 for atom notation, the subscript met is related to methyl groups).

| **Compound** | **$(BTMA)_2[PtCl_6]$** | **$(BTMA)[AuCl_4]$** | **$(BTMA)_2[CuCl_4]$** | **$(BTMA)_2[CuBr_4]$** | **$BTMA^+$ in $H_2O$** |
|---|---|---|---|---|---|
| Method | X-ray | X-ray | X-ray | X-ray | MP2 |
| Bond lengths [Å] | | | | | |
| C1–C2 | 1.393(5) | 1.392(3) | 1.396(4)/1.392(4) | 1.391(6)/1.393(7) | 1.399 |
| C2–C3 | 1.392(5) | 1.389(3) | 1.386(5)/1.389(4) | 1.388(7)/1.370(7) | 1.393 |
| C3–C4 | 1.383(6) | 1.379(4) | 1.382(5)/1.381(5) | 1.379(8)/1.379(7) | 1.395 |
| C4–C5 | 1.383(6) | 1.380(4) | 1.384(4)/1.386(6) | 1.388(7)/1.379(7) | 1.395 |
| C5–C6 | 1.385(5) | 1.379(3) | 1.388(4)/1.390(4) | 1.377(7)/1.402(6) | 1.393 |
| C6–C1 | 1.395(5) | 1.388(3) | 1.394(4)/1.384(4) | 1.391(7)/1.383(6) | 1.399 |
| C1–C7 | 1.505(5) | 1.500(3) | 1.503(4)/1.502(4) | 1.497(6)/1.511(6) | 1.495 |
| C7–N | 1.521(4) | 1.532(2) | 1.527(4)/1.530(4) | 1.528(5)/1.532(5) | 1.516 |
| N–$C_{met}$ | 1.488(4) | 1.508(3) | 1.494(4)/1.499(4) | 1.499(5)/1.493(6) | 1.488 |
| | 1.518(4) | 1.499(3) | 1.502(4)/1.498(4) | 1.507(6)/1.507(6) | 1.490 |
| | 1.492(4) | 1.497(3) | 1.500(4)/1.500(4) | 1.504(5)/1.495(6) | 1.488 |
| Bond angles [deg] | | | | | |
| C1–C2–C3 | 120.6(3) | 119.9(2) | 120.1(3)/120.3(3) | 120.5(5)/120.2(4) | 120.3 |
| C2–C3–C4 | 120.1(4) | 120.4(2) | 120.1(3)/120.2(3) | 120.2(4)/120.7(5) | 120.0 |
| C3–C4–C5 | 119.6(3) | 119.8(2) | 120.2(3)/119.9(3) | 119.5(5)/119.5(4) | 119.9 |
| C4–C5–C6 | 120.8(4) | 120.1(2) | 120.1(3)/119.8(3) | 120.4(5)/120.7(4) | 120.0 |
| C5–C6–C1 | 120.3(3) | 120.6(2) | 120.0(3)/120.7(3) | 120.7(4)/119.0(4) | 120.3 |
| C6–C1–C2 | 118.7(3) | 119.1(2) | 119.4(3)/119.1(3) | 118.6(4)/119.9(4) | 119.3 |
| C2–C1–C7 | 120.6(3) | 119.8(2) | 119.9(3)/120.5(3) | 120.7(4)/119.5(4) | 120.3 |
| C6–C1–C7 | 120.4(3) | 121.0(2) | 120.7(2)/120.4(3) | 120.6(5)/120.6(4) | 120.3 |
| C1–C7–N | 115.3(2) | 114.7(2) | 114.0(2)/113.3(2) | 113.9(3)/113.9(3) | 113.9 |
| C7–N–$C_{met}$ | 111.1(3) | 110.6(2) | 111.2(2)/109.2(2) | 111.5(3)/111.3(3) | 111.1 |
| | 106.8(2) | 107.6(2) | 107.2(2)/107.6(2) | 107.7(3)/107.4(3) | 107.4 |
| | 111.9(2) | 112.1(2) | 111.2(2)/111.0(2) | 110.7(3)/111.2(3) | 111.1 |
| Dihedral angles [deg] | | | | | |
| C1–C2–C3–C4 | −1.1(5) | −1.0(4) | −0.5(5)/0.5(5) | 0.8(7)/0.6(7) | 0.0 |
| C2–C3–C4–C5 | 1.0(6) | 0.1(4) | 0.0(5)/−1.6(5) | −1.9(7)/−1.5(7) | 0.0 |
| C3–C4–C5–C6 | −0.3(5) | 0.2(4) | −0.2(5)/0.7(5) | 0.4(7)/0.9(6) | 0.0 |
| C4–C5–C6–C1 | −0.3(5) | 0.4(4) | 1.0(5)/1.3(5) | 2.3(7)/0.5(6) | 0.0 |
| C6–C1–C2–C3 | 0.5(5) | 1.6(3) | 1.3(5)/1.5(5) | 1.9(7)/0.8(6) | 0.0 |
| C3–C2–C1–C7 | 174.8(3) | 178.6(2) | 179.0(3)/−177.1(3) | −178.3(4)/179.8(4) | 179.7 |
| C2–C1–C7–N | 90.7(4) | 89.8(3) | 92.0(3)/92.2(3) | 94.2(5)/91.6(5) | 90.7 |
| C1–C7–N–$C_{met}$ | 71.6(3) | 63.0(2) | 62.5(3)/63.7(3) | 65.6(4)/68.9(5) | 61.0 |
| | −167.5(3) | −177.7(2) | −178.4(3)/−177.4(2) | −175.6(3)/−172.3(4) | 180.0 |
| | −51.8(4) | −57.8(2) | −59.7(3)/−58.4(3) | −56.2(5)/−53.8(5) | −61.0 |

The overlay of the X-ray structure of $BTMA^+$ in $(BTMA)_2[PtCl_6]$ and the MP2-optimized ones in vacuum and in aqueous solutions is shown in Figure 16. The differences between them can be explained as above. A quantitative measure of similarity between two or more structures is the root mean square deviation (RMSD) of their corresponding atomic positions (i.e., the average distance between the corresponding atoms of superimposed molecules). The data in Table 4 confirm that the similarity between the X-ray and both MP2-optimized structures is significantly lower than that between the MP2-optimized structures in vacuum and in aqueous solution.

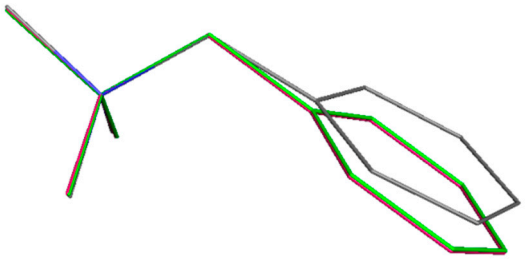

**Figure 16.** Overlay of the X-ray structure of the benzyltrimethylammonium cation in $(C_{10}H_{16}N)_2[PtCl_6]$ (C—gray, N—blue) and of its DFT-optimized structures in vacuum (green) and in aqueous solution (magenta). H-atoms have been omitted for the sake of clarity.

**Table 4.** RMSDs of the corresponding $BTMA^+$ atomic positions in $(C_{10}H_{16}N)_2[PtCl_6]$ and MP2 calculations [Å].

| | |
|---|---|
| MP2 optimized in vacuum vs. X-ray structure | 0.131 |
| MP2 optimized in solvent vs. X-ray structure | 0.130 |
| MP2 optimized in vacuum vs. in solution | 0.006 |

The energies and locations of the highest occupied molecular orbital (HOMO) and the lowest unoccupied molecular orbital (LUMO) are crucial for the chemical reactivity of compounds. According to the Fukui rules [54,55], the locations where the HOMO electron density is largest are most readily attacked by electrophilic or oxidizing reagents. Analogously, the locations of the maximal LUMO density are most probably attacked by nucleophilic or reducing reagents. An additional condition is the suitable orbital energy of the attacking reagent. The energy gap between HOMO and LUMO in $BTMA^+$ is approximately 12 eV, indicating its high stability (Table 5). An aqueous solvent increases the $BTMA^+$ orbital energies and stability. Both HOMO and LUMO (Figures 17 and 18) are located mainly at the phenyl ring. It can be expected that in the case of basic $BTMA^+$ degradation [19–21,56], the attacking $OH^-$ anion is subsequently transferred to the C7 site and the tetramethylammonium group is split.

**Table 5.** MP2 molecular orbital energies of HOMO, $\varepsilon_{HOMO}$, and LUMO, $\varepsilon_{LUMO}$, and their difference, $\Delta\varepsilon$, in $BTMA^+$ in various environments.

| Environment | Vacuum | Aqueous Solution |
|---|---|---|
| $\varepsilon_{HOMO}$ [eV] | −12.66 | −9.28 |
| $\varepsilon_{LUMO}$ [eV] | −0.70 | 3.01 |
| $\Delta\varepsilon$ [eV] | 11.96 | 12.28 |

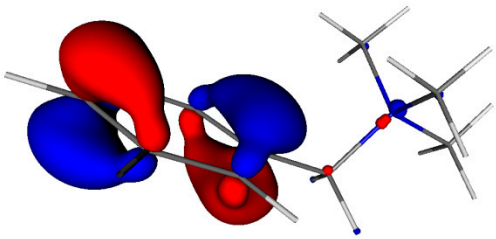

**Figure 17.** HOMO of $BTMA^+$ in aqueous solution (drawn at 0.07 a.u. isosurface).

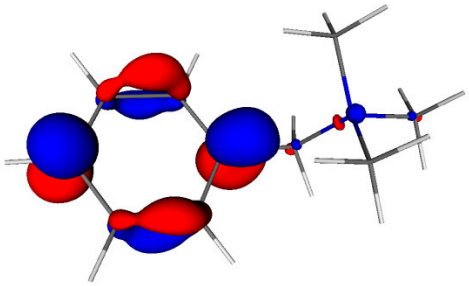

**Figure 18.** LUMO of $BTMA^+$ in aqueous solution (drawn at 0.07 a.u. isosurface).

Additionally, active sites of $BTMA^+$ can be deduced on the basis of its electrostatic potential map (Figure 19). As expected, negative potential values are observed at the aromatic phenyl $\pi$ ring. The positive potential at hydrogen atoms explains the less-preferred formation of $H_2O$ molecules under $OH^-$ attack [19].

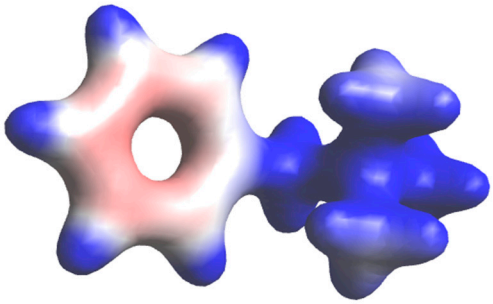

**Figure 19.** Electrostatic potential map of $BTMA^+$ in aqueous solutions (isovalue 0.1 a.u., blue and red colors denote positive and negative values, respectively).

The molecular graph of $BTMA^+$ consisting of atoms, the bond paths between them, and critical points is presented in Figure 20. The corresponding atomic charges and volumes are collected in Table 6. The charges of the phenyl carbons are slightly negative, unlike the positive charges of the aliphatic carbons. Hydrogen charges are slightly positive. The volumes of atoms with the same bonding pattern should be larger for more negatively charged (less positively charged) atoms. This is in contradiction with the lower volumes of the phenyl C atoms in ortho-positions, which indicates their higher reactivity in comparison with the C atoms in the meta- and para-positions. An analogous situation also holds for the phenyl hydrogens.

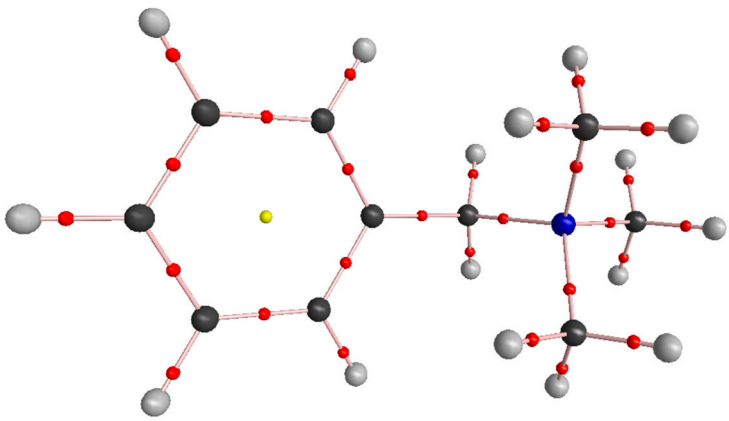

**Figure 20.** Molecular graph of $BTMA^+$ in aqueous solution (C—black, N—blue, H—gray, bond critical points—red, and ring critical point—yellow).

**Table 6.** MP2 atomic charges, q, and volumes, V, of $BTMA^+$ in aqueous solutions (see Figure 1 for atom notation, the subscript met is related to methyl groups).

| | q | V [bohr$^3$] |
|---|---|---|
| C1 | −0.04 | 65 |
| C2 | −0.05 | 80 |
| C3 | −0.05 | 85 |
| C4 | −0.05 | 85 |
| C5 | −0.05 | 85 |
| C6 | −0.05 | 80 |
| C7 | 0.24 | 52 |
| N | −0.98 | 49 |
| $C_{met}$ | 0.25 (3×) | 62 (3×) |
| H2 | 0.07 | 46 |
| H3 | 0.07 | 47 |
| H4 | 0.07 | 47 |
| H5 | 0.07 | 47 |
| H6 | 0.07 | 46 |
| H7 | 0.09 (2×) | 43 (2×) |
| $H_{met}$ | 0.08 (9×) | 44 (9×) |

The selected properties of the $BTMA^+$ bonds are presented in Table 7. Bond strengths can be compared according to electron densities at their bond critical points, $\rho_{BCP}$, or, alternatively, according to the average number of electrons that are shared between bonded atoms (delocalization indices, DI). Both treatments indicate maximal strengths of the phenyl aromatic bonds, whereas the C7–N and N–$C_{met}$ bonds are the weakest ones (even weaker than the C–H bonds). This finding is in agreement with the experimentally observed degradation in basic solutions [19–21,56] connected with the splitting of these weakest bonds, as follows.

$$C_6H_5CH_2N^+(CH_3)_3 + OH^- \rightarrow C_6H_5CH_2OH + N(CH_3)_3 \quad (4)$$

$$C_6H_5CH_2N^+(CH_3)_3 + OH^- \rightarrow C_6H_5CH_2N(CH_3)_2 + CH_3OH \quad (5)$$

**Table 7.** Electron densities, $\rho_{BCP}$, their Laplacians, $\nabla^2\rho_{BCP}$, bond ellipticities, $\varepsilon_{BCP}$, at the BCPs and bond delocalization indices, DI, of $BTMA^+$ in aqueous solution (see Figure 1 for atom notation, the subscript met is related to methyl groups).

| | $\rho_{BCP}$ [e/bohr$^3$] | $\nabla^2\rho_{BCP}$ [e/bohr$^5$] | $\varepsilon_{BCP}$ | DI |
|---|---|---|---|---|
| C1–C2 | 0.3163 | −1.0245 | 0.194 | 1.134 |
| C2–C3 | 0.3196 | −1.0543 | 0.192 | 1.177 |
| C3–C4 | 0.3188 | −1.0507 | 0.187 | 1.173 |
| C4–C5 | 0.3188 | −1.0507 | 0.187 | 1.173 |
| C5–C6 | 0.3196 | −1.0543 | 0.192 | 1.177 |
| C6–C1 | 0.3163 | −1.0245 | 0.194 | 1.134 |
| C1–C7 | 0.2660 | −0.7386 | 0.019 | 0.867 |
| C7–N | 0.2350 | −0.5842 | 0.034 | 0.734 |
| N–$C_{met}$ | 0.2472 (2×) | −0.6567 (2×) | 0.010 (2×) | 0.759 (2×) |
| | 0.2464 | −0.6542 | 0.003 | 0.756 |
| C2–H2 | 0.2930 | −1.1807 | 0.012 | 0.830 |
| C3–H3 | 0.2940 | −1.1901 | 0.012 | 0.843 |
| C4–H4 | 0.2940 | −1.1902 | 0.012 | 0.844 |
| C5–H5 | 0.2940 | −1.1901 | 0.012 | 0.843 |
| C6–H6 | 0.2930 | −1.1807 | 0.012 | 0.830 |
| C7–H7 | 0.2945 (2×) | −1.1864 (2×) | 0.019 (2×) | 0.790 (2×) |
| $C_{met}$–$H_{met}$ | 0.295 (2×) | −1.19 (9×) | 0.024 (9×) | 0.80 (2×) |
| | 0.294 (7×) | | | 0.81 (7×) |

All bonds in $BTMA^+$ have negative values of BCP Laplacians of electron density, $\nabla^2\rho_{BCP}$, which are typical for covalent bonds. Their values reflect the various polarities of individual bond types.

Bond ellipticities, $\varepsilon_{BCP}$, reflect the double-bond π character of individual bonds. We can see that the ellipticities of the phenyl aromatic bonds are approximately one order higher than their σ bond counterparts (single C1–C7, C7-N, N-$C_{met}$, and all C-H bonds).

## 4. Conclusions

In summary, we successfully obtained four salts of benzyltrimethylammonium, namely, bis(benzyltrimethylammonium) hexachloroplatinate (**1**), benzyltrimethylammonium tetrachloroaurate (**2**), bis(benzyltrimethylammonium) tetrachlorocuprate (**3**), and bis(benzyltrimethylammonium) tetrabromocuprate (**4**). Interestingly, in **1**, the anion is completed by inversion symmetry. Overall, the synthetized salts demonstrate varied supramolecular features arising from different anionic species. However, high similarity is observed in the **3** and **4** crystals. The supramolecular systems of the investigated salts, driven by only non-classical interactions, were thoroughly explored using diverse modern computational approaches.

Hirshfeld surface analysis and enrichment ratio calculations indicate that C···H/H···C interactions contribute prominently to the stabilization of all supramolecular assemblies. In addition, Cl···H/H···Cl and Cu···H/H···Cu interactions have relevance in **1**–**3**, and in **3**–**4**, respectively. Br···H/H···Br, Br···C/C···Br interactions are favorable in **4**. The hierarchy of synthons was examined using extended Hirshfeld surface analysis, 2D fingerprint plots, enrichment ratio, and energy framework calculations. As a result, a library of hydrogen-bonding motifs was constructed. Equivalent synthons were identified that may serve as interchangeable motifs in the design of derivatives with controllable features. A bifurcated synthon $R^1_2(6)$ between cation and anion is present in all four crystals.

Our MP2 calculations pointed out differences between the structures in solutions and the solid-state structures affected by intermolecular interactions. The $C_s$ symmetry point group is preserved in solutions, which is reflected in the symmetry of their electronic structural characteristics. Frontier molecular orbitals (HOMO and LUMO), the electrostatic potential map, and electron structure knowledge enable the explanation of $BTMA^+$ reactivity and its active sites.

The long-distance ordering in a crystal resembles the local ordering in a liquid [57]. In liquid solutions, a short-range order of solvent molecules persists, and the solvent molecules move in the potential field of the solute ions or molecules. The liquid solvent contains regions with ordered bonds of a regular lattice as well as regions with non-ordered molecules in a random array. Its dynamic behavior with short rotational and translational correlation times indicates high bond-exchange rates. Solvent effects can affect chemical reactions (reaction rate, mechanism, and selectivity), chemical equilibria (relative stability of ions and transition states), and physical properties (solubility, crystal shape, and shifts in spectral lines).

This article has been completed while Sepideh Jafari, the fifth author, was the Doctoral Candidate in the Interdisciplinary Doctoral School at Lodz University of Technology, Poland.

**Supplementary Materials:** The following supporting information can be downloaded at https://www.mdpi.com/article/10.3390/cryst15121051/s1. Figure S1: Equivalent/interchangeable H-bonding synthons observed in the analyzed crystals **1**–**4** (X1, X2 = Cl, Br). Figure S2: Crystal packing similarity between **3** (green) and **4** (orange). Figure S3: Upper: Percentage contributions of inter-contacts in crystals **1**–**4** (above 1%)—calculations for entire salt; Below: fingerprint plots for overall interactions for **1**–**4**. Figure S4: Energy framework calculations for cations in **1**. Figure S5: Energy framework calculations for cations in **3**. Figure S6: Energy framework calculations for cations in **4**. Table S1: Bond lengths for **1**. Table S2: Valence angles for **1**. Table S3: Torsion angles for **1**. Table S4: Bond lengths for **2**. Table S5: Valence angles for **2**. Table S6: Torsion angles for **2**. Table S7:

Bond lengths for **3**. Table S8: Valence angles for **3**. Table S9: Torsion angles for **3**. Table S10: Bond lengths for **4**. Table S11: Valence angles for **4**. Table S12: Torsion angles for **4**. Table S13: ΠI-based inter-contacts in **1**–**4** (<4 Å). Table S14: Aromatic Analyser results. Table S15: Library of H-bonding synthons (<20-membered) in **1**–**4**. Table S16: Enrichment ratios for cations in **1** (>0.9). Table S17: Enrichment ratio for cation no. 1 in **3** (>0.9). Table S18: Enrichment ratio for cation no. 2 in **3** (>0.9). Table S19: Enrichment ratio for cation no. 1 in **4** (>0.9). Table S20: Enrichment ratio for cation no. 2 in **4** (>0.9). Table S21: The total interaction energies for **1**–**4** via energy framework calculations.

**Author Contributions:** Conceptualization, A.M. and J.B.; methodology, M.B., J.B., A.M. and D.T.; validation, D.T. and J.B.; formal analysis, J.B., D.T. and M.B.; investigation, D.T., J.B., A.M., M.B., I.D.M., K.W., S.J. and I.J.; data curation, D.T., K.W. and J.B.; writing—original draft preparation, J.B., D.T., M.B. and A.M. All authors have read and agreed to the published version of the manuscript.

**Funding:** This research has been supported by the Slovak Scientific Grant Agency VEGA (project no. 1/0175/23).

**Data Availability Statement:** CCDC 2464968–2464971 contain the supplementary crystallographic data for this paper, accessed on 17 June 2025. These data can be obtained free-of-charge via https://www.ccdc.cam.ac.uk/structures.

**Acknowledgments:** The authors thank the HPC center at the Slovak University of Technology in Bratislava, which is a part of the Slovak Infrastructure of High-Performance Computing (SIVVP project ITMS 26230120002, funded by European Region Development Funds) for the computational time and resources made available.

**Conflicts of Interest:** The authors declare no conflicts of interest.

## References

1. Hasan, M.; Kozhevnikov, I.V.; Siddiqui, M.R.H.; Steiner, A.; Winterton, N. Gold compounds as ionic liquids. Synthesis, structures, and thermal properties of N, N '-Dialkylimidazolium tetrachloroaurate salts. *Inorg. Chem.* **1999**, *38*, 5637–5641. [CrossRef]
2. Yamamoto, K.; Inada, S. Liquid-liquid distribution of ion associates of tetrahalogenoaurate (III) with quaternary ammonium counter ions. *Anal. Sci.* **1995**, *11*, 643–649. [CrossRef]
3. Kawasaki, H.; Uota, M.; Yoshimura, T.; Fujikawa, D.; Sakai, G.; Arakawa, R.; Kijima, T. Self-Organization of Surfactant−Metal-Ion Complex Nanofibers on Graphite Surfaces and Their Application to Fibrously Concentrated Platinum Nanoparticle Formation. *Langmuir* **2007**, *23*, 11540–11545. [CrossRef]
4. Tkacheva, A.; Sharutin, V.; Sharutina, O.; Shlepotina, N.; Kolesnikov, O.; Shishkova, Y.S.; Peshikova, M. Tetravalent platinum complexes: Synthesis, structure, and antimicrobial activity. *Russ. J. Gen. Chem.* **2020**, *90*, 655–659. [CrossRef]
5. Xie, D.; Xu, J.; Cheng, H.; Wang, N.; Zhou, Q. The role played by amine and ethyl group in the reversible thermochromic process of $[(C_2H_5)_2NH_2]_2CuCl_4$ probing by FTIR and 2D-COS analysis. *J. Mol. Struct.* **2018**, *1161*, 267–272. [CrossRef]
6. Mande, H.M.; Ghalsasi, P.S.; Navamoney, A. Synthesis, structural and spectroscopic characterization of the thermochromic compounds $A_2CuCl_4$:[(Naphthyl ethylammonium)$_2CuCl_4$]. *Polyhedron* **2015**, *91*, 141–149. [CrossRef]
7. Gilmore, B.F.; Andrews, G.P.; Borberly, G.; Earle, M.J.; Gilea, M.A.; Gorman, S.P.; Lowry, A.F.; McLaughlin, M.; Seddon, K.R. Enhanced antimicrobial activities of 1-alkyl-3-methyl imidazolium ionic liquids based on silver or copper containing anions. *New J. Chem.* **2013**, *37*, 873–876. [CrossRef]
8. Kaur, G.; Kumar, S.; Dilbaghi, N.; Bhanjana, G.; Guru, S.K.; Bhushan, S.; Jaglan, S.; Hassan, P.; Aswal, V. Hybrid surfactants decorated with copper ions: Aggregation behavior, antimicrobial activity and anti-proliferative effect. *Phys. Chem. Chem. Phys.* **2016**, *18*, 23961–23970. [CrossRef]
9. Li, D.; Zhao, X.-M.; Zhao, H.-X.; Long, L.-S.; Zheng, L.-S. Coexistence of magnetic-optic-electric triple switching and thermal energy storage in a multifunctional plastic crystal of trimethylchloromethyl ammonium tetrachloroferrate (III). *Inorg. Chem.* **2018**, *58*, 655–662. [CrossRef]
10. Hayashi, S.; Saha, S.; Hamaguchi, H. A new class of magnetic fluids: Bmim [fecl/sub 4/] and nbmim [fecl/sub 4/] ionic liquids. *IEEE Trans. Magn.* **2006**, *42*, 12–14. [CrossRef]
11. Desiraju, G.R. Crystal engineering: A holistic view. *Angew. Chem. Int. Ed.* **2007**, *46*, 8342–8356. [CrossRef]
12. Aakeröy, C.B.; Champness, N.R.; Janiak, C. Recent advances in crystal engineering. *CrystEngComm* **2010**, *12*, 22–43. [CrossRef]
13. Bojarska, J.; Łyczko, K.; Breza, M.; Mieczkowski, A. Recurrent Supramolecular Patterns in a Series of Salts of Heterocyclic Polyamines and Heterocyclic Dicarboxylic Acids: Synthesis, Single-Crystal X-ray Structure, Hirshfeld Surface Analysis, Energy Framework, and Quantum Chemical Calculations. *Crystals* **2024**, *14*, 733. [CrossRef]

14. Bojarska, J.; Łyczko, K.; Mieczkowski, A. Synthesis, Crystal Structure and Supramolecular Features of Novel 2, 4-Diaminopyrimidine Salts. *Crystals* **2024**, *14*, 133. [CrossRef]
15. Bojarska, J.; Łyczko, K.; Mieczkowski, A. Novel Salts of Heterocyclic Polyamines and 5-Sulfosalicylic Acid: Synthesis, Crystal Structure, and Hierarchical Supramolecular Interactions. *Crystals* **2024**, *14*, 497. [CrossRef]
16. Lian, L.; Zhang, P.; Gao, J.; Zhang, D.; Zhang, J. Self-assemblies of isomeric copper iodide trimers with geometry-dependent photophysical properties. *Chem. Mater.* **2023**, *35*, 9339–9345. [CrossRef]
17. Mączka, M.; Gągor, A.; Stroppa, A.; Gonçalves, J.N.; Zaręba, J.K.; Stefańska, D.; Pikul, A.; Drozd, M.; Sieradzki, A. Two-dimensional metal dicyanamide frameworks of BeTriMe [$M(dca)_3(H_2O)$] (BeTriMe = benzyltrimethylammonium; dca = dicyanamide; M = $Mn^{2+}$, $Co^{2+}$, $Ni^{2+}$): Coexistence of polar and magnetic orders and nonlinear optical threshold temperature sensing. *J. Mater. Chem. C* **2020**, *8*, 11735–11747. [CrossRef]
18. Maczka, M.; Ptak, M.; Trzebiatowska, M.; Kucharska, E.; Hanuza, J.; Palka, N.; Czerwinska, E. THz, Raman, IR and DFT studies of noncentrosymmetric metal dicyanamide frameworks comprising benzyltrimethylammonium cations. *Spectrochim. Acta Part A-Mol. Biomol. Spectrosc.* **2021**, *251*, 119416. [CrossRef]
19. Chempath, S.; Boncella, J.M.; Pratt, L.R.; Henson, N.; Pivovar, B.S. Density functional theory study of degradation of tetraalkylammonium hydroxides. *J. Phys. Chem. C* **2010**, *114*, 11977–11983. [CrossRef]
20. Sturgeon, M.R.; Macomber, C.S.; Engtrakul, C.; Long, H.; Pivovar, B.S. Hydroxide based benzyltrimethylammonium degradation: Quantification of rates and degradation technique development. *J. Electrochem. Soc.* **2015**, *162*, F366. [CrossRef]
21. Karibayev, M.; Myrzakhmetov, B.; Kalybekkyzy, S.; Wang, Y.; Mentbayeva, A. Binding and degradation reaction of hydroxide ions with several quaternary ammonium head groups of anion exchange membranes investigated by the DFT method. *Molecules* **2022**, *27*, 2686. [CrossRef]
22. McCrum, I.; Hickner, M.; Janik, M. Quaternary ammonium cation specific adsorption on platinum electrodes: A combined experimental and density functional theory study. *J. Electrochem. Soc.* **2018**, *165*, F114. [CrossRef]
23. Guan, K.; Tao, L.; Yang, R.; Zhang, H.; Wang, N.; Wan, H.; Cui, J.; Zhang, J.; Wang, H.; Wang, H. Anti-corrosion for reversible zinc anode via a hydrophobic interface in aqueous zinc batteries. *Adv. Energy Mater.* **2022**, *12*, 2103557. [CrossRef]
24. Wang, T.; Zheng, D.; Zhang, Z.; Wang, L.; Zhang, J. Exploration of catalytic species for highly efficient preparation of quinazoline-2,4(1H, 3H)-diones by succinimide-based ionic liquids under atmospheric pressure: Combination of experimental and theoretical study. *Fuel* **2022**, *319*, 123628. [CrossRef]
25. Bonamico, M.; Dessy, G.; Vaciago, A. The crystal structure of bis-trimethylbenzylammoniumtetrachlorocuprate (II). *Theor. Chim. Acta* **1967**, *7*, 367–374. [CrossRef]
26. Jin, L.; Liu, N.; Li, Y.-J.; Wu, D.-H. Bis (benzyltrimethylammonium) tetrabromidocuprate (II). *Struct. Rep.* **2011**, *67*, m1325. [CrossRef]
27. Jin, Y.; Yu, C.-H.; Zhang, W. Structural diversity of a series of chlorocadmate (II) and chlorocuprate (II) complexes based on benzylamine and its N-methylated derivatives. *J. Coord. Chem.* **2014**, *67*, 1156–1173. [CrossRef]
28. CrysAlis, C. *CrysAlis Red. Xcalibur PX Software*, version 1.171.40.67a; Oxford Diffraction Ltd.: Abingdon, UK, 2008.
29. Clark, R.; Reid, J. The analytical calculation of absorption in multifaceted crystals. *Found. Crystallogr.* **1995**, *51*, 887–897. [CrossRef]
30. Sheldrick, G.M. Crystal structure refinement with SHELXL. *Acta Crystallogr. C Struct. Chem.* **2015**, *71 Pt 1*, 3–8. [CrossRef]
31. Sheldrick, G.M. SHELXT–Integrated space-group and crystal-structure determination. *Found. Crystallogr.* **2015**, *71*, 3–8. [CrossRef]
32. Head-Gordon, M.; Pople, J.A.; Frisch, M.J. MP2 energy evaluation by direct methods. *Chem. Phys. Lett.* **1988**, *153*, 503–506. [CrossRef]
33. Head-Gordon, M.; Head-Gordon, T. Analytic MP2 frequencies without fifth-order storage. Theory and application to bifurcated hydrogen bonds in the water hexamer. *Chem. Phys. Lett.* **1994**, *220*, 122–128. [CrossRef]
34. Frisch, M.; Trucks, G.; Schlegel, H.; Scuseria, G.; Robb, M.; Cheeseman, J.; Scalmani, G.; Barone, V.; Petersson, G.; Nakatsuji, H. *GAUSSIAN09*, version 9.0; Gaussian Inc.: Wallingford, CT, USA, 2011.
35. Marenich, A.V.; Cramer, C.J.; Truhlar, D.G. Universal solvation model based on solute electron density and on a continuum model of the solvent defined by the bulk dielectric constant and atomic surface tensions. *J. Phys. Chem. B* **2009**, *113*, 6378–6396. [CrossRef]
36. Varetto, U. *Molekel*, version 5.4. 0.8; Swiss National Supercomputing Centre: Manno, Switzerland, 2009.
37. Hanwell, M.D.; Curtis, D.E.; Lonie, D.C.; Vandermeersch, T.; Zurek, E.; Hutchison, G.R. Avogadro: An advanced semantic chemical editor, visualization, and analysis platform. *J. Cheminform.* **2012**, *4*, 17. [CrossRef]
38. Bader Richard, F. *Atoms in Molecules: A Quantum Theory*; Oxford University Press: Oxford, UK, 1994.
39. Keith, T.A. *AIMAll*, version 17.11. 14; TK Gristmill Software: Overland Park, KS, USA, 2017.
40. Biegler-Konig, F.; Schonbohm, J.; Bayles, D. *Software News and Updates-AIM2000-A Program to Analyze and Visualize Atoms in Molecules*; John Wiley & Sons Inc.: New York, NY, USA, 2001; pp. 545–559.
41. Schrödinger, L. *The AxPyMOL Molecular Graphics Plugin for Microsoft PowerPoint*, version 1.8; Schroedinger, LLC: New York, NY, USA, 2015.

42. Kabsch, W. A solution for the best rotation to relate two sets of vectors. *Found. Crystallogr.* **1976**, *32*, 922–923. [CrossRef]
43. Turner, M.; McKinnon, J.; Wolff, S.; Grimwood, D.; Spackman, P.; Jayatilaka, D.; Spackman, M. *CrystalExplorer*, version 17.5; University of Western Australia: Crawley, Australia, 2017.
44. Spackman, M.A.; Jayatilaka, D. Hirshfeld surface analysis. *CrystEngComm* **2009**, *11*, 19–32. [CrossRef]
45. Jelsch, C.; Ejsmont, K.; Huder, L. The enrichment ratio of atomic contacts in crystals, an indicator derived from the Hirshfeld surface analysis. *IUCrJ* **2014**, *1*, 119–128. [CrossRef]
46. Spackman, P.R.; Turner, M.J.; McKinnon, J.J.; Wolff, S.K.; Grimwood, D.J.; Jayatilaka, D.; Spackman, M.A. CrystalExplorer: A program for Hirshfeld surface analysis, visualization and quantitative analysis of molecular crystals. *Appl. Crystallogr.* **2021**, *54*, 1006–1011. [CrossRef]
47. Mackenzie, C.F.; Spackman, P.R.; Jayatilaka, D.; Spackman, M.A. CrystalExplorer model energies and energy frameworks: Extension to metal coordination compounds, organic salts, solvates and open-shell systems. *IUCrJ* **2017**, *4*, 575–587. [CrossRef]
48. Grimme, S. Semiempirical GGA—type density functional constructed with a long—range dispersion correction. *J. Comput. Chem.* **2006**, *27*, 1787–1799. [CrossRef]
49. Macrae, C.F.; Sovago, I.; Cottrell, S.J.; Galek, P.T.; McCabe, P.; Pidcock, E.; Platings, M.; Shields, G.P.; Stevens, J.S.; Towler, M. Mercury 4.0: From visualization to analysis, design and prediction. *Appl. Crystallogr.* **2020**, *53*, 226–235. [CrossRef]
50. Wood, P.A.; Olsson, T.S.; Cole, J.C.; Cottrell, S.J.; Feeder, N.; Galek, P.T.; Groom, C.R.; Pidcock, E. Evaluation of molecular crystal structures using Full Interaction Maps. *CrystEngComm* **2013**, *15*, 65–72. [CrossRef]
51. Bernstein, J.; Davis, R.E.; Shimoni, L.; Chang, N.L. Patterns in hydrogen bonding: Functionality and graph set analysis in crystals. *Angew. Chem. Int. Ed. Engl.* **1995**, *34*, 1555–1573. [CrossRef]
52. Etter, M.C. Encoding and decoding hydrogen-bond patterns of organic compounds. *Acc. Chem. Res.* **1990**, *23*, 120–126. [CrossRef]
53. Tan, S.L.; Jotani, M.M.; Tiekink, E.R. Utilizing Hirshfeld surface calculations, non-covalent interaction (NCI) plots and the calculation of interaction energies in the analysis of molecular packing. *Struct. Rep.* **2019**, *75*, 308–318. [CrossRef]
54. Fukui, K.; Yonezawa, T.; Nagata, C.; Shingu, H. Molecular orbital theory of orientation in aromatic, heteroaromatic, and other conjugated molecules. *J. Chem. Phys.* **1954**, *22*, 1433–1442. [CrossRef]
55. Fukui, K. Role of frontier orbitals in chemical reactions. *Science* **1982**, *218*, 747–754. [CrossRef]
56. Long, H.; Pivovar, B.S. Hydroxide degradation pathways for substituted benzyltrimethyl ammonium: A DFT study. *ECS Electrochem. Lett.* **2015**, *4*, F13. [CrossRef]
57. Reichardt, C.; Welton, T. *Solvents and Solvent Effects in Organic Chemistry*; Wiley Online Library: Hoboken, NJ, USA, 2011.